Journal of Hydrology 616 (2023) 128699

Contents lists available at ScienceDirect

Journal of Hydrology

journal homepage: www.elsevier.com/locate/jhydrol

Research papers

Drivers of spatiotemporal patterns of surface water inputs in a catchment at the rain-snow transition zone of the water-limited western United States

K. Hale [a,b,*], L. Kiewiet [c], E. Trujillo [d,e], C. Krohe [f,g], A. Hedrick [e], D. Marks [e], P. Kormos [h], S. Havens [e,i], J. McNamara [d], T. Link [j], S.E. Godsey [g,j]

[a] Department of Geography, University of Colorado, Boulder, CO, USA
[b] Institute of Arctic and Alpine Research, University of Colorado, Boulder, CO, USA
[c] Department of Ecosystem Science and Sustainability, Colorado State University, Fort Collins, CO, USA
[d] Department of Geosciences, Boise State University, Boise, ID, USA
[e] Northwest Watershed Research Center, USDA Agricultural Research Service, Boise, ID, USA
[f] Ramboll US Consulting Inc., Vancouver, WA, USA
[g] Department of Geosciences, Idaho State University, Pocatello, ID, USA
[h] NOAA-NWS Colorado Basin River Forecast Center, Salt Lake City, UT, USA
[i] Snowbound Solutions LLC, Boise, ID, USA
[j] Department of Forest, Rangeland and Fire Sciences, University of Idaho, Moscow, ID, USA

ARTICLE INFO

This manuscript was handled by Marco Borga, Editor-in-Chief, with the assistance of Massimiliano Zappa, Associate Editor

Keywords:
Snow
Snowmelt
Water balance
Energy balance
Rain-on-snow events
Hydrological modeling
Climate warming
Recharge

ABSTRACT

Spatial and temporal dynamics of rainfall and snowmelt (i.e., surface water inputs, SWI) control soil moisture, groundwater recharge, and streamflow at annual, seasonal, and event scales. In the rain-snow transition zone, comprising a large portion of the mountainous western United States, there is limited understanding of the sensitivity of spatiotemporal SWI dynamics across hydrologically variable water years (WYs). We modeled rainfall and snowpack dynamics in a small headwater catchment (1.8 km^2) spanning the rain-snow transition in southwestern Idaho, USA, for two hydrologically distinct WYs (2011 and 2014). In wet WY 2011 and dry WY 2014, total precipitation drove spatial variability in annual SWI. Snow drifts generated more SWI (901–2080 mm) than high-elevation scour zones (442–640 mm), which generated less SWI than mid-elevation, non-drift locations (452–784 mm). Seasonally, energy fluxes differed most during the snowmelt period, where higher net radiation at lower elevations and south-facing slopes drove SWI production. At the rain-on-snow (ROS) event scale, higher elevations and north-facing slopes generated 15–20 % of annual SWI, due mainly to higher turbulent fluxes. The most productive ROS events occurred after peak snow water equivalent (SWE), when rainfall fell onto ripe snowpacks. Snow drift locations were less susceptible to melt during ROS events, offset by the larger cold content and snowpack mass. Thus, catchment water resources depend on SWI magnitude, location, and timing, which are moderated by drift persistence at all temporal scales. As the climate warms, shifts in spatiotemporal SWI distribution are expected with declines in snowfall and snowfall redistribution in this area.

1. Introduction

During winter and spring, the spatial transition between rainfall and snowfall in the mountainous western United States (US) can result in a jagged line separating white-covered terrain above and snow-free surfaces below. The elevation of the snow line might change with aspect and over time, and vary with air temperatures and incoming precipitation (Klos et al., 2014; Mote et al., 2018). This affects the timing of infiltration and runoff of rainfall and snowmelt, with cascading effects on catchment ecohydrological cycles including evapotranspiration (Kraft and McNamara, 2021), and growing season duration (Poulos et al., 2021). Comparing the spatiotemporal distribution of rainfall and snowmelt across water years helps to reveal which water balance components are most sensitive to different hydroclimatic conditions.

The rain-snow transition zone has previously been defined as areas that receive at least 7 % of total annual precipitation as mixed rainfall and snowfall precipitation events (Kormos et al., 2018), and, following this definition, covers approximately 40 % of the mountainous

* Corresponding author at: Department of Geography, University of Colorado, 4001 Discovery Drive, Boulder, CO 80303, USA.
E-mail address: kaha3050@colorado.edu (K. Hale).

https://doi.org/10.1016/j.jhydrol.2022.128699
Received 4 March 2022; Received in revised form 13 October 2022; Accepted 20 October 2022
Available online 10 November 2022

landscape in the western US (Klos et al., 2014). Because winter season temperatures in this area fluctuate around 0 °C (Jennings et al., 2018), the snowpack often melts intermittently in parts of the catchment (Kormos et al., 2014a) and is susceptible to small changes in atmospheric conditions, including warming and shifts in precipitation magnitude and phase (Seyfried et al., 2021; Williams et al., 2009). The distribution of rainfall and snowmelt is thus heterogeneous in the rain-snow transition zone (Kormos et al., 2014a). And while this is true in most regions that experience snowfall, the precipitation in the rain-snow transition zone is often more variable, because the physical phase of precipitation (i.e., liquid as rainfall or solid as snowfall) can vary at fine scales (Klos et al., 2014).

Hydrologic characteristics within the rain-snow transition zone might exemplify future climatic effects at higher, currently snow-dominated elevations (Fyfe et al., 2017; Klos et al., 2014; Nayak et al., 2010). The observed snowline has already begun to creep toward higher elevations in recent decades as the rain-snow transition zone has shifted upward, reducing snow-covered area and the number of snow-covered days at lower elevations, affecting the timing and amount of available downstream water (Hamlet et al., 2005; Regonda et al., 2005). Across the western US, peak seasonal snowpack storage, measured as snow water equivalent (SWE) around April 1, has declined substantially over the last half century (Mote et al., 2005, 2018; Regonda et al., 2005), accompanied by an earlier onset of spring due to increased winter and spring temperatures (Folland et al., 2001; Marshall et al., 2019a; Musselman et al., 2017; Steward et al., 2005). Variability in SWE magnitude and in peak SWE timing are expected to increase, particularly in regions where rainfall may replace snowfall near the rain-snow transition (Marshall et al., 2019b).

Another anticipated change with climate warming is more frequent rain-on-snow (ROS) events (Beniston and Stoffel, 2016; Cohen et al., 2015; Lo´pez-Moreno et al., 2013, 2021; Musselman et al., 2018). At the current rain-snow transition zone, ROS events already occur frequently, especially at low- to mid-elevations (Lo´pez-Moreno et al., 2013; Shi and Liu, 2021). During these events, relatively warm rain transfers energy (as advected heat) into the relatively cold snowpack (McCabe et al., 2007). When this happens, positive sensible and latent heat fluxes dominate the snowpack energy balance (Marks et al., 1998), and can lead to early-season snowmelt and flooding as well as late-season drought (Guan et al., 2016). Warmer, shallower snowpacks are more vulnerable to increased energy inputs during ROS events (Nolin and Daly, 2006; Brunengo, 2012), which can rapidly increase snowmelt in a short period of time (Beniston and Stoffel, 2016; Julander and Clayton, 2018). Climatic changes may lead to complex shifts in snowmelt responses during ROS events (Musselman et al., 2018). Melt from ROS events may also be limited if the snowpack is so shallow that it completely melts early during such events (Würzer et al., 2016; Kroczynski, 2004). In contrast, if the snowpack remains consistently deep under warming conditions, but rain events are more intense, more energy may be added into the snowpack via advection or turbulent fluxes, leading to more heterogeneous hydrologic responses than previously observed (Osterhuber, 1999; Würzer et al., 2016). Snowmelt and energetic responses may also vary across the watershed during ROS events, challenging the expectation that ROS events will always generate large amounts of water output (Garvelmann et al., 2015, Kormos et al., 2014b; Marks et al., 1998; Wever et al., 2014; Würzer et al., 2016).

To anticipate changes in future water availability from both rainfall and snowmelt, we must improve our understanding of the sensitivity of catchments in the rain-snow transition zone to the current range of water and energy inputs (Harpold et al., 2017). Reported hydrologic patterns and catchment responses typically reflect average spatial and temporal conditions in mostly snow-dominated regions (Mote et al., 2018). This leaves a notable gap in our understanding of catchment and sub-catchment hydrologic sensitivity to changes in water and energy inputs at the rain-snow transition across different timescales, and during hydroclimatically different years. In addition, the sensitivities of particular catchments, as in our case, Johnston Draw, Idaho, USA, may reflect responses to both static (i.e., relatively constant, such as underlying landscape) and dynamic (i.e., changing, such as wind characteristics and effects) controls (Godsey et al., 2018).

How defined static and dynamic controls modulate the distribution and driving processes of precipitation inputs can be investigated by simulating the spatiotemporal distribution of snowpack and snowmelt. The sum of rainfall and snowmelt at the soil surface is referred to as the surface water inputs (SWI), which summarize the timing and amount of water entering the terrestrial system (Klos et al., 2014; Kormos et al., 2018). The spatial distribution of SWI likewise depends on precipitation magnitude, resulting in SWI variability across aspects and elevations as well as between scour and drift locations, where snowfall has been preferentially deposited or transported by wind (Kiewiet et al., 2022; Kormos et al., 2014a; Lehning et al., 2008; Luce et al., 1998). The spatiotemporal distribution of SWI might also be impacted by additional static boundary conditions such as vegetation and slope, and dynamic boundary conditions, including energy fluxes (Kormos et al., 2014a; Pomeroy et al., 2003). Because SWI influences soil moisture, streamflow, groundwater recharge, plant productivity and nutrient cycling (Kormos et al., 2014a; McNamara et al., 2005), quantifying the primary drivers of the spatiotemporal patterns of SWI will allow us to understand the impact that SWI has on these fundamental processes, stores, and fluxes. And as SWI distributions change in a warming climate (Hale et al., 2022), the subsequent distribution of water availability will certainly be further impacted.

Previous research suggests that the drivers of SWI may vary annually, seasonally, and on the event scale. Annually, SWI distribution in the snow-dominated Upper Sheep Creek catchment was affected by snow drifting and aspect differences, with snowpacks persisting longer into the spring season in drift locations and on northeast-facing slopes (Luce et al., 1998). Seasonally, SWI timing and amount have been shown to vary across aspects in the rain-snow transition zone (Kormos et al., 2014a). However, the combined effects of elevation, snowfall redistribution, and differences in inter-annual hydrologic behavior have not yet been evaluated in the rain-snow transition zone, but are likely prevalent across such regions (Klos et al., 2014).

Further, at the ROS event scale, catchment-average precipitation and snowpack characteristics have been related to stream discharge (Rücker et al., 2019; Würzer et al., 2016), but the spatial origin of SWI during these events has not yet been quantified. Past studies have collectively shown that the drivers of SWI vary inter- and intra-annually but have focused only on single time scales (e.g., annual, or seasonal, or event scale). More recently, Godsey et al. (2018) compiled relevant hydrometeorological data in the rain-snow transition and Kiewiet et al. (2022) explored spatially distributed, annual SWI within the rain-snow transition zone across relatively wet, dry, rainy and snowy water years in relation to annual streamflow and stream drying. We aim to build on these works, focusing on the varying drivers of spatially distributed SWI across multiple time scales (annual and seasonal), between multiple years (specifically a wet and a dry year), and during hydrometeorological anomalies (e.g., ROS events), which remain important knowledge gaps, particularly in the dynamic rain-snow transition zone in the western US.

To address these research gaps, we evaluated variations in spatial and temporal SWI, precipitation, snow water equivalent (SWE), and energy fluxes across aspects, elevation bands, and drift and scour locations to identify the drivers of SWI. We evaluated water and energy fluxes annually, seasonally, and across multiple ROS events for two water years (WYs 2011 (wet) and 2014 (dry), defined from October 1 to September 30) in a catchment located in the rain-snow transition zone at Reynolds Creek Experimental Watershed (RCEW). The RCEW was selected as an experimental watershed because of its representativeness of the region (Seyfried et al., 2000, 2001). We used the iSnobal/Automated Water Supply Model (AWSM) (Havens et al., 2020; Marks et al., 1999) at the catchment scale, forced with an extensive hydro-

meteorological dataset (Godsey et al., 2018). The following research questions were addressed for this watershed in the semi-arid, intermountain west rain-snow transition zone: 1a.) How do the spatial patterns of annual surface water inputs (SWI) vary across a wet and a dry year in the rain-snow transition zone? 1b.) Which water or energy balance variables drive these annual spatial patterns, and how do they vary seasonally? 2a.) Where is SWI generated during ROS events in the rain-snow transition zone? 2b.) What inputs or underlying conditions influence SWI at the ROS event scale? The use of the physics-based snow model iSnobal permits us to evaluate these questions with a focus on the physical processes that are representative of SWI production and ROS events across rain-snow transition zones in the intermountain west of the US.

2. Methods

2.1. Study area

This study was conducted in Johnston Draw (Fig. 1A–C), a catchment located in the rain-snow transition within the RCEW. RCEW is part of the Critical Zone Observatory (CZO) network, and located in the Owyhee continental mountain range of southwest Idaho, US, ~100 km southwest of Boise, Idaho and ~30 km east of the Idaho-Oregon border (Fig. 1A). RCEW is managed by the US Department of Agriculture (USDA) Agricultural Research Service (ARS) as a representative watershed in the US intermountain west (Seyfried et al., 2000, 2001) and covers a 239 km^2 area ranging from snow-dominated (Fig. 1B, white), mixed-phase precipitation (Fig. 1B, gray) to rain-dominated (Fig. 1B, black) subcatchments (modified from Godsey et al. (2018)).

Johnston Draw is a 1.8 km^2 headwater catchment within the RCEW, with an average elevation of 1719 m (range of 1497 m–1869 m) (Godsey et al., 2018). The catchment includes an east/west-oriented valley, an east-flowing stream, and opposing north/south-aspect hillslopes (Fig. 1C). Between 2004 and 2014, Johnston Draw experienced a yearly mean temperature of 8.1 °C and mean annual precipitation (MAP) of ~600 mm, where 39 %–53 % of MAP fell as snow (Godsey et al., 2018). Annual runoff ratios ranged from 0.08 to 0.45 (Godsey et al., 2018).

Wind typically comes from the south and southwest, with an annual average wind speed range between 2.8 m s^{-1} across most of the catchment (measured at all but one site, described in Section 2.2) and 4.5 m s^{-1} in the windiest areas (measured at one relatively exposed site, site 124) (Godsey et al., 2018). Wind in Johnston Draw preferentially redistributes and deposits snow from windy scour zones to form drifts in the southwest part of the catchment, which faces predominantly to the northeast. Vegetation on the north-facing slopes includes snowberry (*Symphoricarpos*), big sagebrush (*Artemisia tridentate*), aspen (*Populus tremuloides*) groves and low sagebrush (*Artemisia arbuscula*) with wheatgrass (*Elymus trachycaulus*). South-facing vegetation consists of *Artemisia arbuscula*, *Elymus trachycaulus*, mountain mahogany (*Cercocarpus ledifolius*), and bitter-brush (*Purshia tridentate*) (Godsey et al., 2018; Stephenson, 1970). Under this vegetation, sandy loam soils, with an average depth of 0.96 m, make up the land surface and shallow subsurface of Johnston Draw (Patton et al., 2018).

2.2. Datasets

Eleven stations monitored atmospheric conditions in Johnston Draw and were used to force a snowpack model for this analysis (Fig. 1C). The stations are positioned in the watershed so that one station exists on both the north- and south-facing slopes at roughly the same elevation, every 50 m in elevation from the bottom (east-end) to the top (west-end) of the catchment (Marks et al., 2013; Seyfried et al., 2021; Table 1). Measurements of solar radiation (S_i), wind speed (w_s) and direction (w_d), precipitation (ppt), air temperature (T_a), relative humidity (RH) and snow depth are available at three of these stations (125, 124b, and 124), and measurements of snow depth, T_a and RH are available at the additional eight stations (jdt1, jdt2, jdt2b, jdt3, jdt3b, jdt4, jdt4b, and jdt5, Table 1). All data are available at an hourly resolution (Godsey et al., 2018). A digital elevation model (DEM) is available at 1-m resolution from a 2014 airborne lidar flight (Shrestha and Glenn, 2016).

To evaluate the range of water inputs to Johnston Draw, two WYs were assessed: 2011, a relatively wet year (total annual precipitation = 709 mm, 120 % of MAP), and 2014, a relatively dry year (528 mm, 86 % of MAP). These two water years had very similar mean annual air

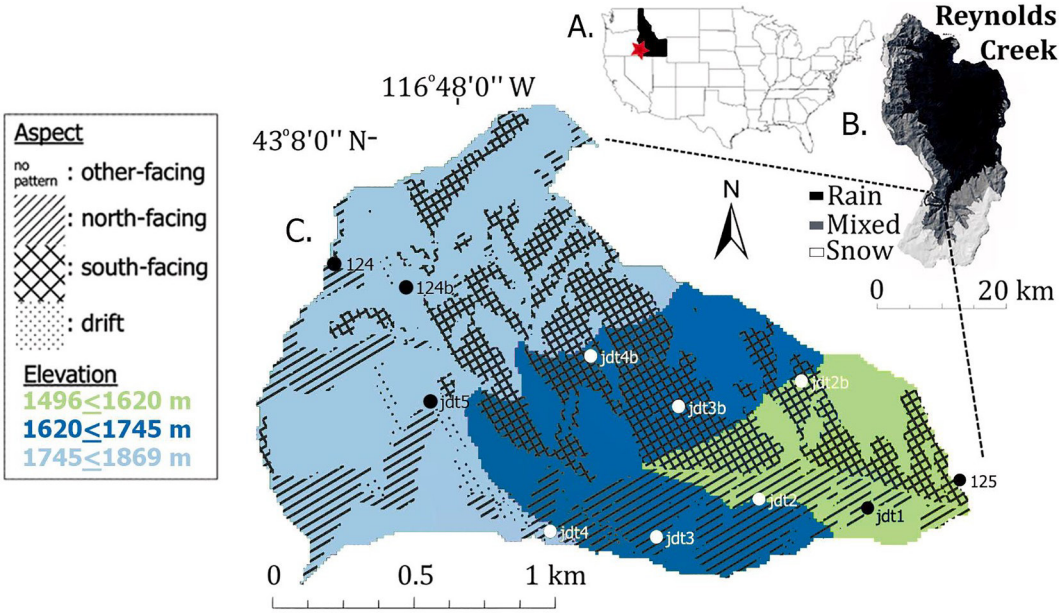

Fig. 1. Located in (A) southwestern Idaho, and part of the (B) Reynolds Creek Experimental Watershed within the mixed-precipitation zone (modified from Godsey et al. (2018)), (C) Johnston Draw is a sub-catchment at the rain-snow transition zone with 11 weather stations and one stream discharge measurement location. For complete data availability at each site, refer to Table 1. The catchment has been divided into low, mid and high elevations (shown by color); north, south and other-facing aspects (shown by hatching pattern); and snow drifts (shown by small black dots). (For interpretation of the references to colour in this figure legend, the reader is referred to the web version of this article.)

Table 1
Elevation, aspect and start dates for all measurement stations, as well as the suite of forcing variables (air temperature (T_a), relative humidity (RH), wind direction (w_d), wind speed (w_s), solar radiation (S_i), wind-corrected (ppt_a) and (ppt_s) precipitation), used within the hydrologic model for water years 2011 (wet) and 2014 (dry) (Godsey et al., 2018). An asterisk indicates the measurements that are taken at each station. Data is available through at least 30 Sep 2014 for all stations. Station 125 is located near the catchment outlet. Stations 124 and 124b are located toward the top of the catchment. Additional stations are labeled as pairs (e.g., "1" and "1b") according to the distance from the catchment output. Pairs exist at similar elevations on opposing aspects (see Fig. 1).

Station	Elev (m)	Aspect	Start Date	T_a/RH	w_d/w_s	S_i	ppt_a	ppt_s
125	1508	SE	1 Oct 2003	*	*	*	*	*
jdt1	1552	N	5 Nov 2005	*				
jdt2b	1611	S	4 Mar 2011	*				
jdt2	1613	N	5 Nov 2005	*				
jdt3	1655	N	21 Sep 2005	*	*			
jdt3b	1659	S	13 Dec 2010	*	*			
jdt4b	1704	S	4 Mar 2011	*	*			
jdt4	1706	N	2 Nov 2005	*				
jdt5	1757	N	2 Nov 2005	*	*			
124b	1778	SE	11 Nov 2006	*	*	*		*
124	1804	NE	1 Oct 2003	*	*	*	*	*

temperatures (0.2 °C difference), yet the differences in precipitation contributed to a ~4× difference in discharge (Kiewiet et al., 2022). In addition, one large ROS event along with multiple smaller ROS events occurred in both water years, making these WYs suitable to evaluate SWI generation at event and annual time scales.

2.3. Modeling

We used the iSnobal/Automated Water Supply Model (AWSM), which was developed at the USDA Agricultural Research Service (ARS) in Boise, ID, to estimate catchment snow water supply (Havens et al., 2020; Marks et al., 1999). AWSM standardizes the steps needed to: 1) distribute weather station data using the Spatial Modeling for Resources Framework (SMRF, Havens et al., 2018, 2020), 2) run the energy and mass balance model, iSnobal, as described below (Marks et al., 1999), and 3) compile the results as user-friendly output (Havens et al., 2018, 2020).

Hourly meteorological data (precipitation, air temperature, solar radiation, vapor pressure, wind speed and direction) are distributed in SMRF via the elevation gradient presented in the digital elevation model (DEM) (Havens et al., 2020). iSnobal, a physics-based spatially distributed energy- and mass-balance snow model, then generates spatially distributed SWE and SWI (Marks et al., 1999). iSnobal is driven by the distributed meteorological and precipitation data to model the snowpack evolution throughout the accumulation and ablation seasons across a gridded spatial domain (e.g., a watershed). iSnobal represents the snowpack as two layers: a surface layer that is in contact with the air and a bottom layer that is in contact with the soil (Marks et al., 1999). The mass and energy balance terms and fluxes are tracked for both snow layers, and each layer is presumed to be homogeneous (Garen and Marks, 2005). iSnobal uses the spatially distributed meteorological forcings listed in Table 1 to solve the energy and mass balance at each snow-covered grid cell (e.g., 10 m × 10 m). The snowpack energy balance is expressed as:

$$\Delta Q = \sum (Rn + H + LE + G + M)\Delta t \quad (1)$$

where ΔQ = the change in snowpack energy storage (W m^{-2}), t is time (s), R_n = net radiation (W m^{-2}, includes shortwave and longwave fluxes), H = sensible heat flux (W m^{-2}), LE = latent heat flux (W m^{-2}), G = snow/soil heat exchange (W m^{-2}), M = advected heat from precipitation (W m^{-2}). The change in energy state of the snowpack depends on whether the average snowpack temperature is at or below the freezing temperature:

$$\begin{aligned} &\text{If snowpack temperature} < 0\ ^{\circ}\text{C}: \Delta Q = \Delta Q_{melt} \\ &\text{If snowpack temperature} = 0\ ^{\circ}\text{C}: \Delta Q = \Delta Q_{melt} \end{aligned} \quad (2)$$

Q_{cc} is commonly known as the cold content and is the total energy required to raise the temperature of the snowpack to 0 °C:

$$Q_{cc} = -c_i \cdot \rho_w \cdot h_{swe} \cdot (T_s - T_m) \quad (3)$$

and Q_{melt} is the energy associated with phase change:

$$Q_{melt} = (h_{swe}) \cdot \rho_w \cdot \gamma_f \quad (4)$$

where c_i is the heat capacity of ice (2102 J kg^{-1} K^{-1}), T_s is the average temperature of the snowpack (°C), T_m is the melting point of ice (0 °C), ρ_w is the density of water (approximately 1000 kg m^{-3}), h_{swe} is the snow water equivalent (m), and γ is the latent heat of fusion (3.34 × 10^6 J kg^{-1}).

At each time step, Δt, iSnobal calculates mass and energy exchanges at the interfaces between the snowpack and the atmosphere, and between the snowpack and the underlying soil surface. In addition, the model computes the snowpack temperature, mass, snow depth, SWE, and snow coverage for the watershed. During a model run, when additional energy is added to the snowpack and exceeds a specified liquid water content threshold (1 % of SWE volume), iSnobal calculates melt based on the available energy (Eq. (4)) (Marks et al., 1999; Marks and Winstral, 2001). Liquid water leaving the snowpack at the base is calculated after considering snowpack water holding capacity and refreezing. This mass output is then recorded as SWI. After each time step, iSnobal readjusts the structural (e.g., SWE and depth) and thermal snowpack properties of each layer (Kumar et al., 2013). Finally, iSnobal computes various energy fluxes within the snowpack (Havens et al., 2020). Here, we considered five components of the energy balance: latent heat, sensible heat, heat from the interaction between the snowpack and soil, advected energy (heat that enters the snowpack as precipitation), net radiation, and the sum of all energy balance terms. These components were then compared to the cold content of the snowpack (variables listed and defined in Table 2).

We ran the model at a 10-m resolution, which was coarse enough to smooth small-scale variations in topography, but fine enough to capture the processes that drive differential melt. We relied on the well-established interannual consistency in snow distributions (Pflug and Lundquist, 2020; Schirmer et al., 2011; Sturm and Wagner, 2010) to rescale interpolated precipitation and snowfall fields using the Vo¨egeli et al. (2016) approach, for both simulated years, using one available lidar snow depth survey near peak snowpack conditions (March 2009) (Tinkham et al., 2014). The Vo¨egeli et al. (2016) approach implicitly captures the spatial heterogeneity of snow using distributed snow depth information (e.g., from lidar or structure from motion) and assimilates this information into physically based models such as iSnobal/AWSM. Thus, this methodology was used to rescale precipitation to represent the redistribution of snowfall by wind and topographic effects, leading to the development of drifts and scour areas in the Johnston Draw catchment. In this way, we reproduced the observed snowpack

Table 2
List of the AWSM model output variables that were included in the annual analysis. Variables are listed as water fluxes or energy fluxes.

Flux	Variable	Units	Definition
Water	Total precipitation	mm	Total precipitation (rainfall and snowfall)
	Mean SWE	mm	Average annual snow water equivalent
Energy	Sum of energy balance	W m^{-2}	Sum of all energy balance variables of the surface and ground snow layers
	Net radiation	W m^{-2}	Sum of all surface energy balance variables
	Sensible heat	W m^{-2}	Turbulent energy flux related to the temperature change of a substance
	Latent heat	W m^{-2}	Turbulent energy flux related to the phase change of a substance
	Advected precipitation	W m^{-2}	Energy transferred from precipitation, particularly as rainfall
	Snow soil	W m^{-2}	Energy entering (+) or leaving (−) the snowpack at the soil/snow interface
	Cold content	MJ m^{-2}	The amount of energy required to create an isothermal snowpack and eventually induce melt

distribution patterns while conserving the initial mass estimation. Despite a relatively dense array of 11 meteorological stations (described in Section 2.2 and listed in Table 1), precipitation rescaling was found to improve the representation of the catchment-wide snowpack (Kiewiet et al., 2022; Trujillo et al., 2019). The precipitation rescaling approach was implemented only when snowfall was present because wind is a dominant control on snow redistribution, especially in Johnston Draw (Marks et al., 1998; Molotch et al., 2011; Winstral et al., 2002). Consequently, we expected the spatial distribution of SWI to partially reflect the spatial distribution of snowfall and total precipitation resulting from this rescaling approach. The limitations presented by this approach, including the rescaling, model choice, available datasets, and their potential uncertainties, are discussed in Section 4.3.1.

Finally, the iSnobal model was run hourly with the rescaled precipitation as an input. Model-generated snow thicknesses were verified spatially against lidar snow depths (R^2: 0.88) and temporally against snow depth time series at each of the meteorological stations (median Nash-Sutcliffe Efficiency (NSE): 0.65) (see Kiewiet et al. (2022) for a detailed description of the model performance and related uncertainties).

2.4. Relationship between spatially-distributed SWI and water and energy balance variables across temporal scales

To evaluate the spatial and temporal drivers of SWI in Johnston Draw at the annual, seasonal, and ROS event scales across the two different WYs, we quantified precipitation, SWE, SWI, and snowpack energy balance variables (listed and described in Table 2). The methodology for determining the drivers of SWI at each temporal scale is described in the following paragraphs.

Annually, correlation analyses were conducted using 11 aspect-elevation bins to cluster grid cells into north-facing, south-facing and other-facing areas (neither south- nor north-facing, thus either east- or west-facing or flat) at low-, mid- and high-elevations, as well as drift locations at mid- and high-elevations (shown in Fig. 1C and listed in Table 3). Drifts were defined as grid cells with annual peak SWE in the top 10 % within the catchment, which were validated against available observation lidar data (Kiewiet et al., 2022). The aspects of the catchment were calculated from the DEM where north-facing was defined between 330° and 30° and south-facing between 150° and 210°. Other-facing includes all remaining degree values and locations where the slope is <5°. The elevation bins were assigned by dividing the full catchment elevation range into three equal parts. Thus, the elevation bin

Table 3
Simulated basin and aspect-elevation bin averages (precipitation and SWI) and maximum values (SWE) for 2011 and 2014. Low, mid, and high refer to elevation bands (with associated elevation ranges listed). Values at south-facing (SF), other-facing (OF, neither north- nor south-facing), north-facing (NF) aspects, and drifts are listed separately.

		Mean precipitation (mm)		Max SWE (mm)		Mean SWI (mm)	
Year		2011	2014	2011	2014	2011	2014
Catchment average		709	528	897	401	692	520
Low (1496–1620 m)	SF	605	440	125	39	598	435
	OF	837	560	140	42	822	551
	NF	870	579	150	59	856	573
Mid (1620–1745 m)	SF	569	447	135	36	561	442
	OF	788	566	149	67	771	558
	NF	799	572	149	62	784	566
	Drift	1424	901	748	343	1383	898
High (1745–1869 m)	SF	554	459	128	46	540	452
	OF	657	505	150	71	640	497
	NF	593	481	85	58	576	472
	Drift	2080	1265	897	401	1886	1257

labels (low = 1496<1620 m, mid = 1620<1745 m and high = 1745<1869 m) are relative to the catchment elevation range (i.e., "high" refers to locally high elevations). We calculated total annual precipitation and SWI and mean SWE during the snow season, which was defined as the period when snow-covered area >0.0 km^2.

For each of these aspect-elevation bins, we assessed the strength and direction of correlations between SWE, precipitation and SWI. Seasonal variability in SWI, precipitation, SWE and energy balance fluxes was also evaluated by plotting and interpreting time series data, across both water years, using the same 11 aspect-elevation bins. Available spatially distributed topographic variables of slope angle, convexity, elevation, soil type, soil depth, and vegetation height showed no relationship with the spatial distribution of annual and seasonal SWI and were not further considered. Advected energy, a model output, was also not further considered after showing no relationship with spatial SWI distribution.

Finally, at the event scale, we defined ROS events as precipitation events that received more than 5 mm basin-averaged precipitation of which the majority fell as rain (snowfall fraction <0.5), while at least 3 % of the land surface was covered with snow (roughly the areal extent of the defined snow drifts). When periods of rainfall were separated by a dry period of less than 6 h, they were considered a single event. These constraints resulted in a total of seven ROS events in 2011 and nine in 2014. For each event, we calculated the precipitation magnitude (mm) and intensity (mm h^{-1}), event snowfall fraction (unitless), excess SWI (any SWI generated in addition to total event precipitation, mm), snow-covered area (km^2), basin-wide mean SWE (mm) at the start of the event, snowpack cold content (MJ m^{-2}) and liquid water content (mm). When comparing cold content and liquid water content to excess SWI via linear regressions, we normalized each variable by the snow-covered area, to account for the fact that these variables are only calculated for model grid cells where SWE > 0 mm. Thus, the results reflect excess SWI as a product of the grid-cell cold content and liquid water content from only the snow-covered area. Liquid water content, while limited to 1 % of the grid-cell modeled SWE in the model, was used for relative comparisons of snowpack saturation across ROS events. Finally, we assessed whether the date of the event occurred before or after catchment-average peak SWE and quantified the spatial centroid of SWI generation within the catchment. Both the annual average and event-specific centroid locations of SWI generation were calculated and reported as the weighted-average location of SWI. A spatial offset was calculated as any difference between the event-specific SWI centroid

location and the yearly centroid location (2011 or 2014 annual centroids were calculated separately, but were nearly the same).

3. Results

At the 10-m spatial resolution, the modeled snow depths strongly agreed with observational lidar snow depths (R^2: 0.88, see Kiewiet et al., 2022), lending confidence to the use of modeled spatially distributed surface water inputs (SWI) at event to annual scales. To address our specific research questions, we have separated our results by temporal scales: drivers of annual and seasonal scale SWI (research questions 1a and 1b), and drivers of rain-on-snow event SWI (research questions 2a and 2b). At both temporal scales, we address differences between the wet and dry water years; the discussion follows a similar order.

3.1. Drivers of annual and seasonal SWI

3.1.1. Annual scale

Total annual precipitation and mean and peak SWE were greater in 2011 than in 2014 (Table 3): the catchment received 34 % more precipitation in 2011 than in 2014 (catchment mean precipitation: 709 mm vs 528 mm). The snowfall fraction was 14 % greater (0.48 vs 0.34), which equated to 161 mm more snow in 2011 than in 2014 (catchment mean snowfall: 340 vs 179 mm). The higher precipitation inputs resulted in 172 mm more SWI in 2011 than in 2014 (catchment mean SWI: 692 mm vs 520 mm, Fig. 2A & B). In 2011, SWE reached a maximum of 897 mm at the grid-cell scale in the drift locations, whereas maximum SWE was 401 mm in 2014. Peak SWE occurred in similar areas in both years, but exceeded mean catchment precipitation only in 2011 (Table 3). Differences in winter monthly mean air temperatures between the wet and dry years were as follows: 5 °C warmer in 2014 in Nov, 3–6 °C warmer in 2011 in Dec and Jan, 7 °C warmer in 2014 in February, 2 °C warmer in 2014 in March, and equal temperatures in April (see Fig. 2 in Godsey et al., 2018). The mean air temperatures in November–February in these years spanned the 0 °C mark, affecting the phase of falling precipitation and monthly snowfall fraction (Godsey et al., 2018).

Areas of highest annual SWI coincided with snow drifts in the southwestern part of the catchment (Fig. 2A–C), where mean annual SWI in the drift locations ranged from 1383–1886 mm in 2011 and 898–1257 mm in 2014 (Fig. 2D, Table 3). On average, 8.0 % of total annual SWI in 2011 and 6.6 % of total annual SWI in 2014 was generated from the snow drifts. In addition to the large SWI volume generated at the snow drifts, north-facing slopes and other-facing slopes generated more SWI than the south-facing slopes in both water years, especially in 2011 (diamonds, circle-crosses and triangles, respectively, in Fig. 3A & B). Non-drift, high-elevation regions often generated the least amount of SWI in both years due to wind scouring, implicitly represented with the snowfall rescaling approach, compared to the same aspects at lower elevations (Table 3). Differences in precipitation, SWE, and SWI between the two water years were largest at the snow drifts (average ΔSWI of 1130 mm) and north-facing slopes (average ΔSWI of 346 mm) and smaller on the south-facing slopes (Fig. 2C).

At the annual scale, precipitation and SWI were strongly correlated (Fig. 3A & B; R^2 = 0.98 and *p-value* ≤0.05 in both years). In both years, modeled snow drifts received the most redistributed SWE and generated the most SWI (Fig. 3A & B, stars). Higher SWE also occurred in drift locations and north- and other-facing at low elevations, but the relationship with SWI was not as strong (Fig. 3C & D; R^2 = 0.57 and 0.66 in 2011 and 2014, respectively; *p-value* ≤0.05 in both years).

3.1.2. Seasonal scale

Water balance variables: Seasonal differences in SWI across Johnston Draw were a result of snowfall (and thus SWE) and the spatial variability in temporal delays of snowmelt. Although precipitation was rare in Johnston Draw when temperatures were consistently above 0 °C (Jul–Sep) during 2011 and 2014, when it did occur, rainfall was distributed uniformly across all aspect-elevation bins (visible as periods when all lines overlap in Figs. 4A and S1A). In contrast, during December–April in both years, precipitation magnitude varied across the catchment, particularly in drift locations, because snowfall is susceptible to preferential deposition and wind redistribution (Figs. 4A and S1A, elevational lines with the least variability are plotted on top of elevational lines with more variability). The accumulation of snowfall in drifts is clearly visible in the drift SWE time series, as it starkly contrasts with lower SWE in all other aspect-elevation bins (Figs. 4B and S1B).

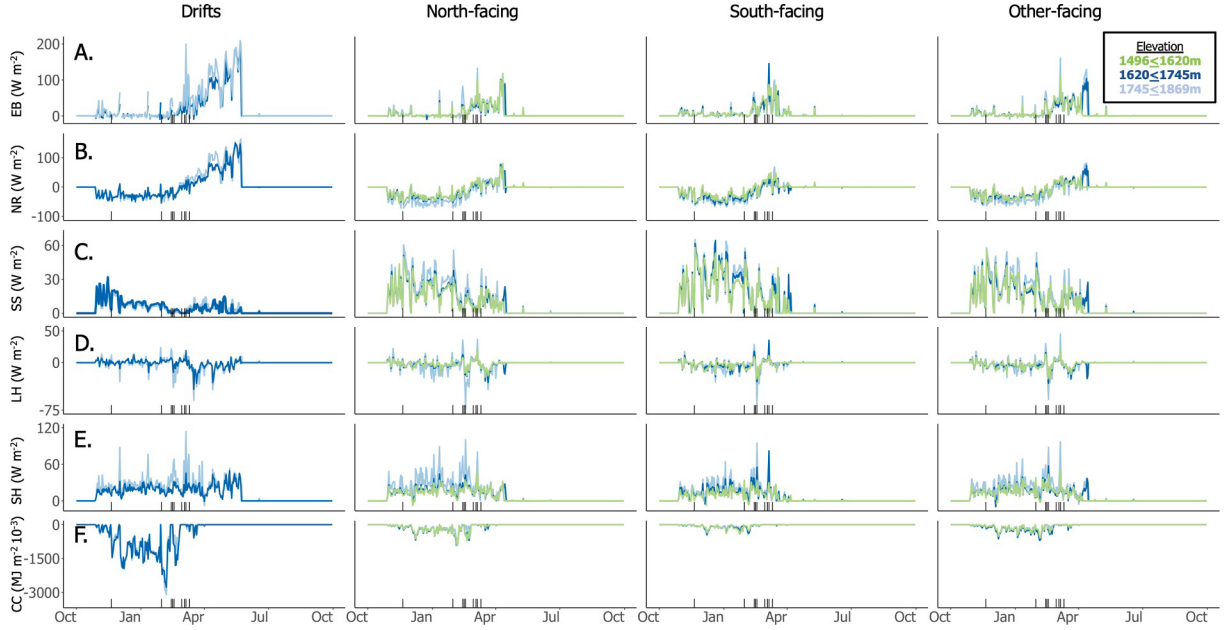

Fig. 2. Total annual SWI in (A) 2011, a relatively wet year (mean ± sd: 692 ± 324 mm); (B) 2014, a relatively dry year (520 ± 175 mm), and (C) the difference in SWI between the two years (SWI 2011–SWI 2014). (D) Boxplots show the variability in annual SWI throughout the watershed in a wet and a dry year. Median total SWI in 2011 (662 mm) was greater than median total SWI in 2014 (494 mm), as was the range and upper extent of outliers.

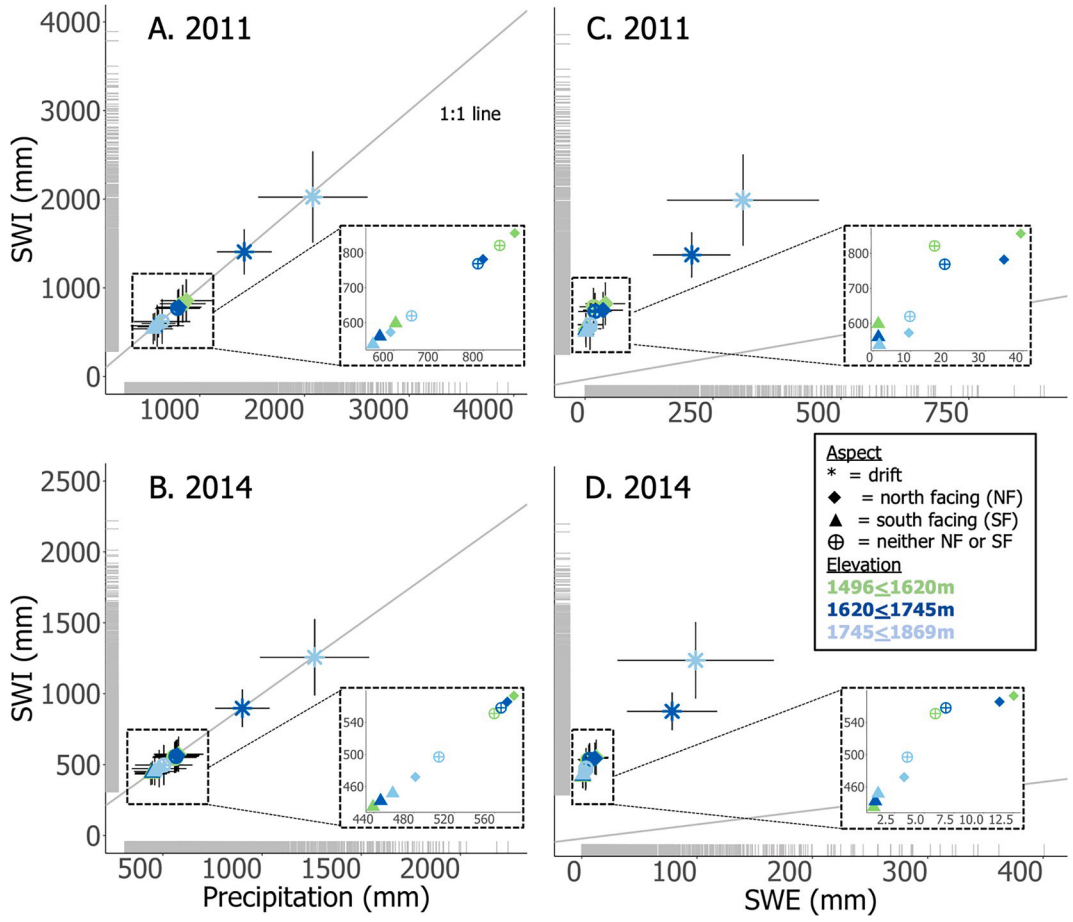

Fig. 3. Correlations between annual SWI and (A) 2011 annual precipitation, (B) 2014 annual precipitation, (C) 2011 mean SWE, and (D) 2014 mean SWE. The points represent the mean value of each variable within each elevation-aspect bin. The gray rug plot along each axis indicates the raw data density and range. Precipitation primarily drives SWI (R^2 = 0.98 in both water years), following close to the 1:1 line (gray diagonal line), as expected by the model interpolation methods and P-SWI relationship.

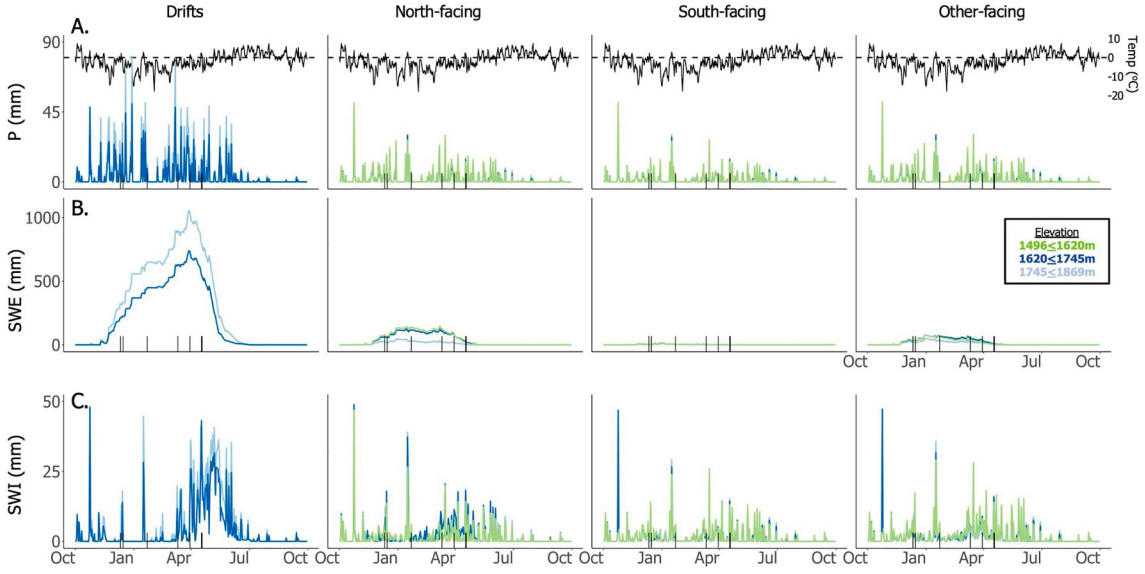

Fig. 4. Water year 2011 water balance fluxes by drift and aspect bins (labeled at the top of each column) (A) Daily precipitation (colored lines, representing the different elevation bins, mm) and temperature (black line ◦C); (B) SWE (mm) and; (C) SWI (mm). Black vertical dashes indicate the date of ROS events during each year (summarized in Table 4), and the black dotted line in figures within panel A indicates 0 ◦C. Lines are layered such that the elevation band with the least variability is plotted on top of those lines with more variability. WY 2014 data is shown in Fig. S1. (For interpretation of the references to colour in this figure legend, the reader is referred to the web version of this article.)

North-facing slopes at low- and mid-elevations had higher seasonal SWE than other-facing regions (Figs. 4B and S1B, "north-facing" and "other-facing"), and the lowest seasonal SWE occurred in the high-elevation, non-drift regions (Figs. 4B and S1B, light blue lines), which is likely due to snow scouring from these regions. Within the low- and mid-elevation bins, the north-facing slopes retained more precipitation as snowfall, and thus SWE.

Daily SWI was often high during the snowmelt period between April and July in both years (maximum daily SWI during snowmelt period: 43 mm in 2011 and 41 mm in 2014, Figs. 4C and S1C, respectively). During this period, on average, SWI was consistently highest in the drift locations, followed by the north-facing slopes, where there was more SWE available to melt. Snowmelt occurred up to two months earlier on south- and other-facing slopes compared to north-facing slopes (i.e., March/April vs May/June in 2011; Figs. 4C and S1C).

Snow cover energy balance components: When and where snowmelt occurred depended on energy fluxes that differed by elevation, aspect, and snowpack accumulation. Until the onset of the ablation season (e.g., April–July in 2011), the overall net energy flux was low (<100 W m^{-2}) in both years and across all aspect-elevation bins (Figs. 5A and S2A), with deviations from the catchment average that were smaller than 5 %. In the latter part of the snowmelt season, the snowpack persisted only in the drift locations, and so the energy balance variables were only calculated in these areas (Havens et al., 2018, 2020). The spatial energy balance patterns were similar across both years (shown for 2011 in Fig. 5 and for 2014 in S2), and differences existed primarily in the magnitude of each energy flux, which was, on average, 15 % larger in 2011, consistent with the deeper snowpack and longer snow season in this year. Thus, differences in energy fluxes between the two years existed near the beginning of snow accumulation and snowmelt periods. The next paragraphs outline the temporal differences in each energy flux in relation to snowmelt generation across aspect-elevation bins and through the two water years.

Net radiation was typically negative in the winter months, and except for drift locations, net radiation was higher at lower elevations (green or dark blue lines, Figs. 5B and S2B) than at higher elevations (light blue lines, Figs. 5B and S2B). Net radiation became positive across all aspects and elevations in March in 2011 (Fig. 5B) and in April in 2014 (Fig. S2B), and continued to increase until the snowpack had fully melted (May–June).

The ground energy flux was noticeably lower in drift locations throughout the mid-winter season, and only exceeded the ground flux of the other aspect-elevation bins after the snowpack had melted from all other areas in the catchment (Figs. 5C and S2C). Between December and April in both years, the ground heat flux was highest on the south-facing slopes and higher at mid- and high elevation relative to the lower elevations.

The latent heat flux was greater in magnitude at higher elevations than at mid- and low elevations (Figs. 5D and S2D). High-elevation latent heat peaked with positive values in December–January and reached its lowest negative values in April–May, when most aspect-elevation bins experienced snowmelt. Latent heat at high elevations became positive again in June. Similarly, the sensible heat flux was most often highest at high elevations (light blue lines, Figs. 5E and S2E), especially on the north-facing aspects during most of the winter months (December–April). Both latent heat and sensible heat fluxes were highest in drift locations only late in the snowmelt period (May–July in both years), as the snowpack had melted from all other aspect-elevation bins.

Lastly, the snowpack cold content was greatest within the thickest snowpacks, which corresponded to drift locations (Figs. 5F and S2F), followed by the north-facing slopes at low and mid-elevations. The shallow snowpacks on the south-facing slopes and high-elevation scour zones were warmest (i.e., a less negative cold content), resulting in earlier melt-out than deeper snowpacks on north-facing slopes and at drift locations. These trends also persisted throughout both water years.

3.2. *Drivers of SWI during ROS events*

Sixteen ROS events were identified and examined (Table 4) during which the catchment received 5–37 mm of precipitation (median: 12 mm) occurring over 9–37 h (median: 22 h). Initial snow-covered area was greater than 5 % of the catchment in all events. The snowfall fraction during these events ranged from 0 to 0.30. Catchment average peak SWE occurred on March 7 in 2011 and February 9 in 2014.

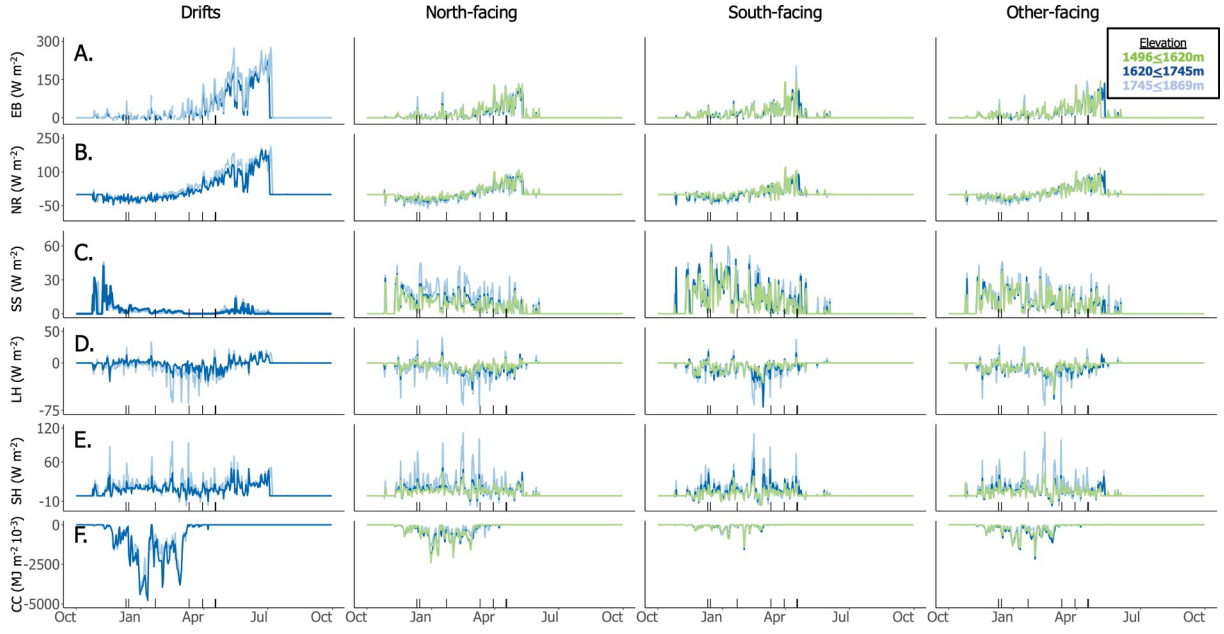

Fig. 5. Water year 2011 energy balance fluxes, by drift and aspect bins (labeled at the top of each column) in W m^{-2}, except for panel (F), which is in $*10^{-3}$ MJ m^{-2}. (A) Daily energy balance (EB), (B) Net radiation (NR), (C) the snow-soil energy flux (SS, energy entering (+) or leaving (−) the snowpack at the soil/snow interface), (D) Latent heat (LH), (E) Sensible heat (SH), and (F) cold content (CC). Gray vertical lines indicate the date of ROS events during the year (summarized in Table 4). 2014 shown in Supplemental Fig. S2: the general patterns across aspects and elevations were similar to 2011, differing only in magnitude. Lines are layered such that the elevation band with the least variability is plotted on top of those lines with more variability.

Table 4
Rain-on-snow (ROS) event characteristics, snowpack characteristics and centroid offset for all ROS event, sorted on the amount of excess SWI generated (SWI_{exc}): event duration (D, hours), snowfall fraction (F_{Snow}), precipitation intensity (P_I, mm h^{-1}), total precipitation (P, mm), SWI (mm), SWI generated in excess of incoming precipitation (SWI_{exc}, mm), cold content of the snowpack (*10^{-3} MJ m^{-2}), fraction of the catchment in which SWI was generated ($F_{Contr.}$), liquid water content of the snowpack (LWC, mm 10^{-3}), snow-covered area (SCA_0, km^2) and SWE at the start of the event (SWE_0, mm) and the offset from the annual SWI centroid in the east-west (ΔX, m) and north-south (ΔY, m) direction, where moving towards the north or east yields a positive offset. Bolded dates are events that occurred after peak SWE.

Date d-mon-y	D (h)	F_{Snow} (–)	P_I (mm h^{-1})	P (mm)	SWI (mm)	SWI_{exc} (mm)	Cold Cont. (*10^{-3} MJ m^{-2})	F_{Contr} (–)	LWC (*10^{-3} mm)	SCA_0 (km^2)	SWE_0 (mm)	ΔX (m)	ΔY (m)
17-Feb-14	23	0	0.3	6.8	0.8	−6	−2.22	0.57	0.93	0.29	34.3	69	53
11-Dec-10	16	0.3	0.54	8.6	4.5	−4.2	−3.51	0.81	0.76	0.38	31.7	104	65
22-Jan-11	9	0	0.82	7.4	4.6	−2.8	−6.52	0.17	3.71	0.36	56.7	73	54
15-Dec-10	11	0	1.49	16.4	14	−2.4	−5.29	0.3	0.07	0.29	28.5	−2	34
20-Nov-13	37	0.14	0.77	28.7	26.7	−2	−1.95	1	0.12	0.42	4.3	−22	28
11-Mar-14	22	0.05	0.84	18.6	16.6	−1.9	−1.90	0.97	0.77	0.07	12.1	24	6
30-Mar-11	14	0	0.39	5.5	4.2	−1.3	−0.56	0.12	45.1	0.14	52.9	54	50
30-Jan-14	33	0.15	0.86	28.3	27.6	−0.7	−3.83	0.5	0.02	0.25	17.2	−67	31
19-Apr-11	21	0.05	0.43	9.1	9.2	0.15	−11.3	1	17.0	0.06	26.2	18	13
17-Apr-11	13	0.08	1.11	14.4	14.7	0.3	−0.78	1	29.9	0.06	27.9	−68	47
04-Mar-14	18	0.08	0.43	7.8	8.7	0.9	−1.16	1	9.02	0.15	23.4	62	−33
28-Feb-14	17	0	0.3	5.1	6.3	1.2	−0.96	0.17	11.3	0.19	28.9	23	−31
15-Feb-14	30	0.27	1.06	31.7	34.7	3	−0.50	1	4.54	0.44	40.2	−39	25
06-Mar-14	34	0.17	0.26	8.7	14.1	5.4	−2.49	1	7.03	0.13	20.9	−21	−45
13-Feb-14	24	0.01	1.15	27.7	33.5	5.8	−0.19	1	10.1	0.65	51.2	−25	46
17-Jan-11	33	0	1.12	37.1	44.3	7.2	−0.35	1	19.8	0.35	61.5	−72	37

Six of the sixteen events occurred before peak SWE (four in 2011, two in 2014) and the remaining ten events occurred after peak SWE. Compared to ROS events occurring after peak SWE, events occurring before peak SWE happened when the pre-event snow-covered area was slightly larger (mean ± sd: 0.34 ± 0.06 km^2 compared to 0.21 ± 0.19 km^2), the snowpack was significantly colder (cold content: 3.58 ± 2.2 *10^{-3} MJ m^{-2} compared to 1.19 ± 0.77 *10^{-3} MJ m^{-2}), and there was slightly more initial SWE (basin-average SWE_0: 33.3 ± 22.2 mm compared to 31.8 ± 13.0 mm).

During the majority of the ROS events, net radiation decreased, but sensible and latent heat fluxes increased (Fig. 5B, D, E and corresponding S2 panels), resulting in energy flux increases during the events (events are shown as black vertical dashes in all Figs. 5 and S2 panels). Specifically, ROS events coincided with an upward or downward spike in latent heat (Figs. 5D and S2D) and increases in sensible heat, particularly at higher elevations (light blue lines in Figs. 5E and S2E).

Different locations in the catchment produced SWI during different ROS events, depending on the initial snowpack and atmospheric conditions, which shifted the catchment centroid location of SWI generation. The annual centroid of SWI in 2011 and 2014 was similar; the difference in centroid location across these years was 30.4 m. Across all events for the two years, the centroid of SWI for individual events extended to 45 m south, 64 m north, 104 m east and 68 m west of the annual SWI centroid (Fig. 6A, Table 4). Spatial offsets from the annual centroid of SWI generation toward the south (i.e., on north-facing slopes, negative ΔY) occurred only during events after peak SWE (triangles in Fig. 6A), and had, on average, smaller snow-covered area at the start of the event (average SCA_0 = 0.15 km^2 compared to 0.28 km^2). SWI centroid offsets toward the east (i.e., lower elevations, positive ΔX) and towards the west (i.e., higher elevations, negative ΔX) were equally divided between events before and after peak SWE (positive versus negative values along x-axis in Fig. 6A). But ROS events with a spatial offset towards the west were, on average, associated with a higher cold content (i.e., warmer snowpack) than ROS events with a spatial offset to the east (average cold content: −1.9 * 10^{-3} MJ m^{-2} compared to −3.5 * 10^{-3} MJ m^{-2}), indicating that thicker snowpacks at higher elevations in the western part of the catchment needed to seasonally warm before generating snowmelt during ROS events. Thus, even during ROS events, snow drifts modulated the timing of basin SWI because they were less susceptible to melt. Finally, events that delivered more than 20 mm of precipitation had a smaller north-south offset from the yearly centroid (mean ± sd ΔY: 23 ± 12 m), compared to events that brought less than 20 mm of precipitation over the basin (ΔY: 29 ± 2 m, Table 4).

The amount of excess SWI (i.e., any SWI in addition to total event precipitation) produced during the ROS events ranged from −6 to +7 mm. Negative excess SWI indicates a net storage of precipitation in the snowpack and/or refreezing, and nearly all ROS events prior to peak SWE resulted in negative excess SWI. Excess SWI depended on the existing snowpack and event-specific characteristics. Two characteristics were typically associated with higher excess SWI generation, though neither relationship was statistically significant: higher liquid water content (Fig. 6B, R^2: 0.26, *p-value* = 0.3) and lower cold content (Fig. 6C, R^2: 0.34, *p-value* = 0.2). On average, however, ROS events occurring after peak SWE (triangles in Fig. 6B & C) generated more excess SWI, corresponding with a warmer snowpack with a higher LWC. Exceptions to this included a few smaller ROS events. Other factors such as basin-average initial SWE (SWE_0), precipitation intensity, and initial snow-covered area (SCA_0) did not appear to independently influence excess SWI production (summarized in Table 4).

The area of the catchment generating SWI during ROS events depended strongly on the season. During events before peak SWE, smaller volumes of SWI were generated on the north-facing slopes and from the snow drifts (Fig. 7A and D), corresponding to centroid offsets to the north (i.e., SWI generated on south-facing slopes). This pattern shifted after basin-average peak SWE, when most SWI was generated on the north-facing slopes (resulting in a centroid offset to the south; Fig. 7B

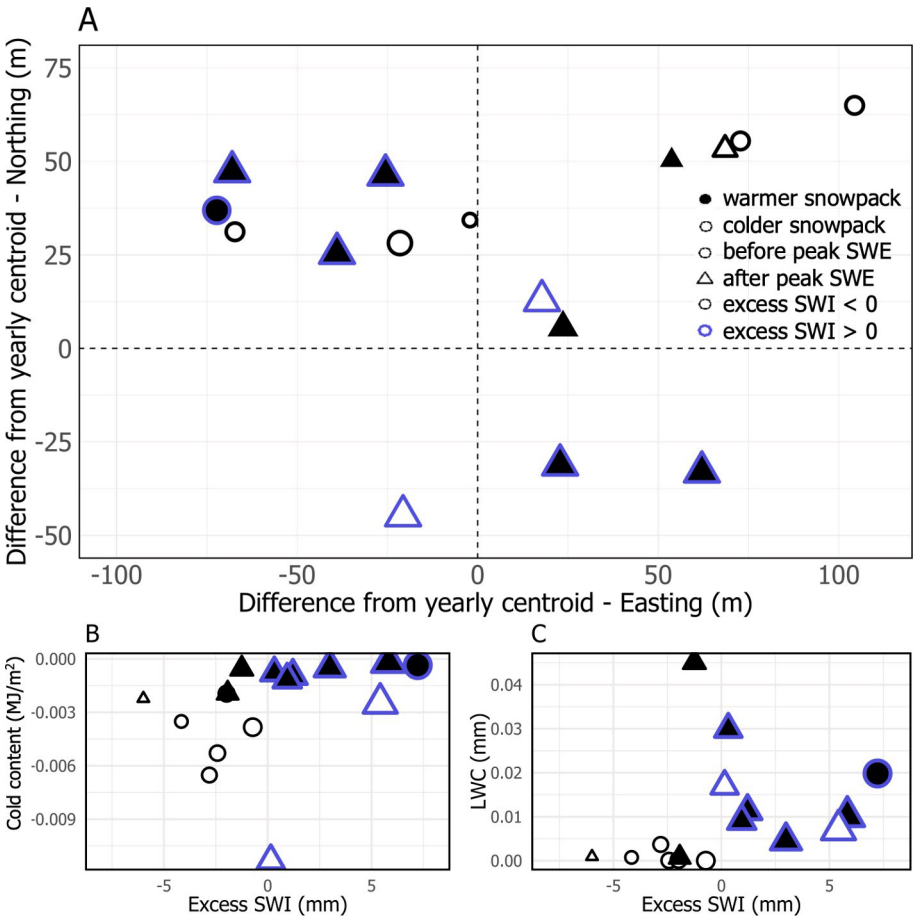

Fig. 6. (A) Offsets relative to the annual SWI centroid of ROS events in both 2011 and 2014 (which differed by ~30 m). Dashed lines indicate no offset from the individual annual centroid of SWI, where each point is thus a difference from the yearly centroid. Positive values indicate offsets that are further east (and thus, lower elevation) or further north (and thus, more south-facing) relative to the centroid location. (B) Excess SWI vs cold content (MJ/m^{-2}, normalized by snow-covered area, $R^2 = 0.34$, $p > 0.05$) and (C) Excess SWI vs snowpack liquid water content (mm, normalized by snow-covered area, $R^2 = 0.26$, $p > 0.05$). To aid the identification of different events, triangles indicate events occurring after peak SWE, circles indicate events occurring before peak SWE, filled (open) symbols indicate events in which the catchment-average snowpack had a cold content above (below) −1.9 MJ m^{-2}, which was the median catchment-average cold content for all studied events. Blue symbol outlines indicate events in which excess SWI > 0 whereas black symbols indicate when SWI was less than total event precipitation. The symbol size indicates the magnitude of excess SWI produced. (For interpretation of the references to color in this figure legend, the reader is referred to the web version of this article.)

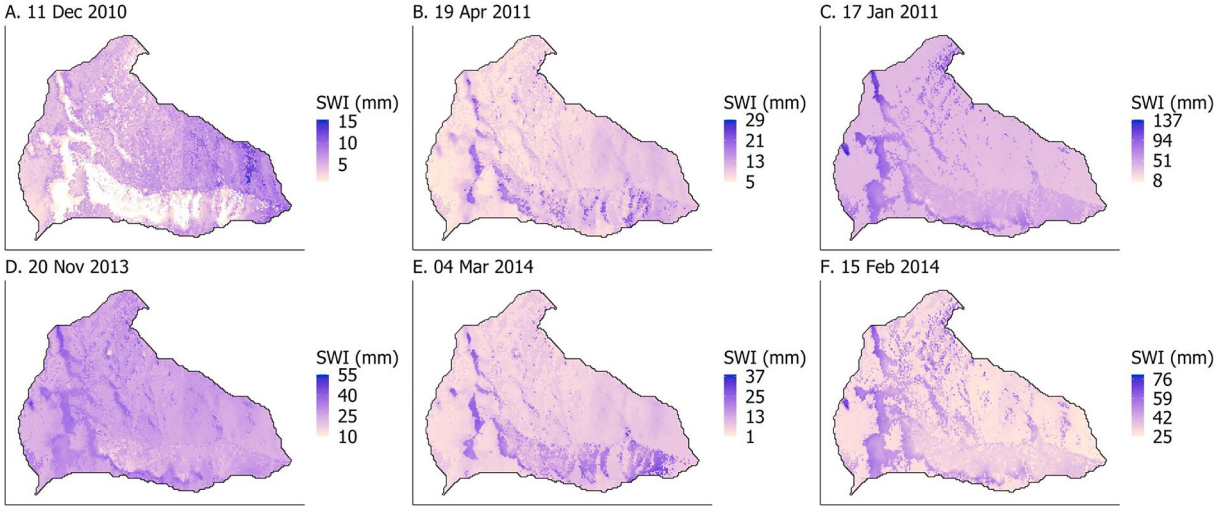

Fig. 7. Maps of surface water inputs (SWI, mm), as rainfall and snowmelt, generated during ROS events in 2011 (A–C) and 2014 (D–F). Across differing SWI magnitudes (see individual color scales), white indicates no SWI generation, beige indicates low amounts of SWI being generated, and blue indicates high amounts of SWI being generated (e.g., rainfall onto the snowpack, inducing snowmelt). The left and center columns show events that occurred before and after peak SWE, respectively. The right column shows the largest event occurring in each year (based on precipitation, duration and SWI produced). (For interpretation of the references to color in this figure legend, the reader is referred to the web version of this article.)

and E). During the large ROS event in 2011 (Fig. 7C), SWI generated on the north-facing slopes and from snow drifts increased with elevation, and differences between snow-covered and snow-free areas were larger than during the largest event of 2014 (Fig. 7C vs F).

4. Discussion

4.1. Annual and seasonal drivers of SWI

4.1.1. Annual scale

In both a wet and a dry water year, the spatial distribution of SWI in Johnston Draw was driven primarily by precipitation magnitude, and the degree of spatial heterogeneity in SWI depended on the phase of precipitation. When precipitation fell as snow, the spatial distribution of precipitation, and thus SWE and SWI, was more heterogeneous than during rainfall events. Accurate representation of high-elevation drift zones adjacent to scour zones required both the elevational and orographic precipitation gradients represented in SMRF (Havens et al., 2018) and the implicit representation of wind redistribution through the snowfall rescaling method by Vo¨egeli et al. (2016) in Johnston Draw (see Section 4.3.1 for further discussion of model assumptions). Together, these results highlight the importance of evaluating SWI beyond calculating the simple catchment-scale average in a rain-snow transition catchment. Because the locations of drifts, scour regions, and aspect-elevation combinations were consistent across relatively wet and dry years, a single study season may reveal the relative spatial pattern of SWI generation, but not its magnitude across a range of climatic conditions. Differences in SWI associated with changing snowfall fraction (the amount of annual precipitation falling as rainfall vs snowfall) was beyond the scope of this work, but has been addressed in a comparison of rainy vs snowy years in this catchment (Kiewiet et al., 2022).

It may be surprising that an accurate snow drift representation is important at the rain-snow transition zone, where the snowpack is shallow and sometimes transient. Indeed, we found that the presence of drifts in this study primarily drove the spatial patterns of SWI, similar to their role in snow-dominated catchments. At higher elevations than the typical rain-snow transition zone, it is well-established that snow drifts significantly affect annual snowmelt (e.g., Anderton et al., 2004; Kretchun et al., 2020; Marshall et al., 2019a; Williams et al., 2009; Winstral et al., 2013). And, although snow drifts in Johnston Draw generated proportionally less SWI than higher-elevation, snow-dominated catchments (e.g., maximum ~3 m of total daily SWI in Upper Sheep Creek compared to maximum ~0.5 m of total daily SWI in Johnston Draw, Fig. 4C) (Marshall et al., 2019a; Winstral et al., 2013), the amount of water stored in the drifts in both a wet and a dry year was substantial (8 %, in 2011, and 6.6 %, in 2014, of total catchment SWI in 3 % of the spatial area) compared to the surrounding landscape. In turn, melt-out dates strongly influence streamflow dry-out dates in Johnston Draw (Kiewiet et al., 2022; Soderquist et al., 2018), emphasizing the importance of capturing snow drifts even in the rain-snow transition zone. Drift representation is important for accurate and informed choices about water resources and adaptation to climate change and variability in snow-influenced regions (Dozier et al., 2016; Luce et al., 1998; Mote et al., 2018).

4.1.2. Seasonal scale

Water balance variables: Whereas rainfall immediately becomes SWI across the catchment, the storage of water in the snowpack delays the generation of SWI in the form of snowmelt for hours to months. In Johnston Draw, the magnitude of this delay depended on the aspect, elevation and depth of the snowpack across the catchment, further emphasizing the need to blend a spatial and temporal analysis of SWI. Notably, we found similar spatiotemporal SWI patterns in both a wet and a dry year: SWI was highest during rainfall and snowmelt events, and snowmelt began on south-facing slopes prior to north-facing slopes and then drifts. Seasonally, SWI was relatively less variable across the catchment at the beginning of the water year because precipitation fell as rain. In early and mid-winter months, snowmelt was generated primarily on south-facing slopes when snow melted on this aspect whereas snowmelt was generated from primarily north-facing and snow drifts slopes in late-winter and spring months from late-season snowmelt. Finally, SWI was again less variable across aspects in summer and early fall months because precipitation fell as rain during those months (Figs. 4C and S1C). Similar to a study during a typical year within a much smaller catchment located to the north (0.015 km^2, (Kormos et al., 2014a)), seasonal to annual SWI generation in Johnston Draw (1.8 km^2) was influenced by both elevation and snow drift locations; this was true during both wet and dry years.

Snow cover energy balance components: Our work extends previous efforts to compare energy fluxes across the rain-snow transition zone by modeling at a spatial scale that is fine enough to capture scour, drift, aspect, and elevation effects. With this detailed comparative approach, we found that energy fluxes in Johnston Draw differed spatially within the year, but the patterns were similar across a wet and dry year with only few exceptions. The largest difference between the two years was a shift in the energy balance due to a more persistent snowpack in the wetter year. Past work exploring the energy balance of SWI production has otherwise typically been limited in space and/or time (Kormos et al., 2014a; Pohl and Marsh, 2006; Shakoor and Ejaz, 2019).

In Johnston Draw, net radiation strongly affected the spatial and temporal patterns of SWI from snowmelt. Low elevations and south- and other-facing slopes had a greater sum of energy fluxes in the entire snowpack, and received more net radiation between January and April, resulting in earlier snowmelt at these locations. Similar to results found in both alpine (Lo´pez-Moreno et al., 2013) and previous rain-snow transition (Kormos et al., 2014a) analyses, net radiation increased on north-facing slopes and at drift locations later in the year (April–June), and continued to increase into the summer months (June–July).

We expected that turbulent heat fluxes would affect Johnston Draw's snowpack throughout the catchment regardless of elevation and aspect, since sensible and latent heat fluxes are known to affect snowmelt across various alpine (Hartman et al., 1999; Prowse and Owens, 1982; Moore and Owens, 1984) and grassland sites (Yang et al., 1999). However, in Johnston Draw, sensible heat fluxes were consistently more positive (i.e., energy entering the snowpack) at higher elevations, whereas latent heat fluxes were more pronounced (i.e., more negative or more positive) at high elevations compared to mid- and low elevations (Fig. 5D & E). These turbulent flux patterns suggest larger variations at locally higher elevations, likely due to higher wind speeds, which might be expected in an area that includes both snow drifts and scour zones. Consistent with Schlo¨gl et al. (2018), the variation of the surface energy fluxes, particularly turbulent fluxes, was larger within modeled complex terrain than for an idealized flat, lower-elevation test site. We did not see obvious seasonal differences in turbulent fluxes across aspects , but we did see differences at drift locations (Fig. 5D & E).

Finally, spatial differences in snowpack thickness greatly influenced the subsequent timing of SWI generation, especially the fraction derived from snowmelt because thicker snowpacks had a greater cold content than shallower snowpacks in Johnston Draw. In turn, these areas required more energy to induce snowmelt, delaying the generation of snowmelt until later in the year (similar to Musselman et al. (2017)). Our results show that relatively consistent spatial cold-content and energy-balance patterns persisted throughout all snow-covered seasons in both water years, until only isothermal snow remained on north-facing slopes and at drift locations (Figs. 5F and S2F). The increased snowpack depth in Johnston Draw was a result of redistributed snowfall due to wind, creating spatiotemporal heterogeneity in the snowpack and its energy balance, and subsequently, SWI derived from snowmelt (Winstral et al., 2013). Without the redistribution of snowfall, cold content of the snowpack and snowmelt timing would be markedly less variable across Johnston Draw.

Under predicted warming, the spatial heterogeneity of SWI will decrease due to decreased snowfall and thus decreased precipitation redistribution, which will lead to decreased thickness and cold content of the catchment snowpack (Mote et al., 2005, 2018; Musselman et al., 2017). These potential changes to the snowpack will increase sensitivity to energy balance variables, and will induce snowmelt earlier in the water year (Musselman et al., 2017, 2021). A change from the historical temporal patterns of SWI in the catchment will ultimately change the timing of water availability that feeds downstream water needs and users (Mote et al., 2005, 2018), increasing water stress later in the season (Knowles et al., 2015). Thus, capturing energy balance effects on SWI patterns across multiple years and at the rain-snow transition zone is critical now and in the future as local and regional snowpacks become more sensitive and are subject to warming and increased interannual variability (Mote et al., 2005, 2018).

4.2. Drivers of SWI during ROS events

The rain-snow transition zone is, by nature, susceptible to ROS events due to its location near the winter snowline (Kormos et al., 2014b). Depending on the temperature and the amount and intensity of rainfall onto the snowpack, large volumes of the snowpack might melt rapidly and, in some situations, generate considerable fluxes of water (Beniston and Stoffel, 2016). The amount of excess SWI produced during the ROS events in Johnston Draw in 2011 and 2014 was small (maximum: 7 mm or ~1 % of annual SWI, Table 4). In Johnston Draw, and consistent with previous work, the development of a ripe snowpack was, on average, an important factor for excess SWI generation during ROS events (Julander and Clayton, 2018; Jennings and Jones, 2015). Exceptions to this averaged relationship included ROS events where initial conditions may have played a compounding role in excess SWI generation (e.g., initial snow-covered area, initial SWE, snow fraction of event). Higher excess SWI often occurred with a higher snow-covered area at the beginning of the ROS event (35 % and 65 % of the catchment was covered in snow prior to the two ROS events where >5 mm of excess SWI was produced, Table 4). The remainder of the catchment experienced precipitation onto bare ground. Finally, after peak SWE, the snowpack present during ROS events was warmer, contained more liquid water, and generated more excess SWI.

Thus, while initial snowpack conditions, including the initial amount of SWE and the snow-covered area, did not correlate strongly with SWI or excess SWI generation, these variables were significantly related to the SWI centroid of each ROS event. In Johnston Draw, upwards of 25 % of total annual SWI was generated during the ROS events, which came from 10 to 100 % of the catchment, from both snow-covered and non-snow-covered grid cells (Table 4). South-facing slopes generated most of the SWI, as both rainfall and snowmelt, during ROS events before peak SWE, where the remaining snowpack on this aspect was often near 0 °C and thus susceptible to melting with added advected energy. North-facing slopes generated most of the SWI, as both rainfall and snowmelt, during ROS events after peak SWE, as the snowpack on this aspect persisted later in the year, allowing for increased snowmelt (i.e., additional SWI production beyond the event precipitation) during these events. In addition, after peak SWE, snow was often no longer present on south-facing slopes, and thus only SWI as rainfall was generated on snow-free aspects.

Unlike the annual and seasonal SWI analyses, during most ROS events snow drifts did not produce substantial SWI since the deeper drifts had a greater cold content and were thus less vulnerable to melt in most rainfall events. The shallower non-drift locations, which produced less SWI at the annual scale, produced more SWI at the ROS event scale. The increased response time between rainfall and SWI production and higher snowpack depths is consistent with past work in both alpine and sub-alpine regions (Jennings and Jones, 2015; Marks et al., 2001; Würzer et al., 2016).

The transient nature of the rain-snow transition zone suggests that, in low and mid-elevation mountain catchments, like Johnston Draw, the snowpack may completely ablate multiple times per winter season, making the timing of excess SWI production less predictable and potentially more frequent, despite lower water storage in the snowpack. This may be especially true under future warming conditions, when the number of ROS events is expected to increase by close to 50 % in mountain and alpine catchments (Beniston and Stoffel, 2016). And, as warming becomes of greater concern in present-day, ROS events have already begun to increase in montane regions (Barnett et al., 2005; Freudiger et al., 2014; Gergel et al., 2017).

Finally, though other studies have found that precipitation intensity and event magnitude are important drivers of snowmelt generation during ROS events, they were not critical drivers of excess SWI production in Johnston Draw. And while rainfall event totals were much lower than peak intensities in other works (e.g., Beniston and Stoffel, 2016), to investigate rainfall thresholds at which more excess SWI may be generated in Johnston Draw, more years, more meteorological variables (e.g., wind, humidity and air temperature) and more ROS events should be considered.

4.3. Assumptions and implications

4.3.1. Assumptions

The assumptions underlying the interpolation methods employed by the AWSM/iSnobal model have critical implications for the precipitation and SWI analyses here, particularly when snowfall occurred. This model was chosen because it is a high-resolution (e.g., 10–100 m), physics-based, spatially distributed model that explicitly simulates SWI, the hydrologic variable of interest (Havens et al., 2020). Precipitation interpolation within AWSM was based on an elevation gradient that led to more precipitation (both snowfall and rainfall) at higher elevations. Because snowfall inputs were rescaled using snow depths from the same lidar observation, small differences between years may have been smoothed, resulting in more spatially similar snowpacks between the two years. Further, the lidar snowfall redistribution pattern, representing peak snow depth from 2009, was used to rescale snowfall at all time steps of year in the model. This limitation forced the assumption that snow drifts form in the same location, regardless of season or event dynamics. This assumption may not always be accurate, leading to model uncertainty. Further, using peak snow depth to redistribute snowfall throughout the entire snow season may overestimate the difference in snowfall between areas with deep vs shallow snowpacks in the catchment. This is due to the imperfect relationship between snowfall and snow on the ground at one snapshot in time. Because portions of the rain-snow transition zone experience intermittent melt (Kormos et al., 2014a), peak snow depth cannot capture snowfall that may have melted earlier in the year, which is more likely in non-drift areas. Thus, the magnitude of differences in snow depth – and thus, spatially distributed SWI magnitude – may be exaggerated across the catchment. To reduce model uncertainty of the snow distribution in Johnston Draw, additional catchment-wide lidar flights accompanied by sufficient on-the-ground observations of the snowpack throughout the snow season and across different years would be valuable.

Subsequently, because only small amounts of precipitation were expected to evaporate or sublimate, SWI strongly reflected spatial and temporal precipitation patterns. Model accuracy, particularly of the redistribution of precipitation (and thus SWI) throughout the two water years of interest, has been shown to be robust (Kiewiet et al., 2022). This accuracy and consistency between years reflects underlying static environmental variables (e.g., topography) and relatively consistent dynamic variables (e.g., wind patterns) that affect the distribution of precipitation and thus SWI (Marks et al., 1998; Molotch et al., 2011; Sta˘hli et al., 1999). Ultimately, while the model results depend on the precipitation redistribution method, this approach is justified at multiple time scales, providing useful insights into the water and energy balance at the rain-snow transition in both wet and dry years. Finally,

while the intent of this work was to explore differences in catchment hydrological response to different weather conditions and water inputs (i.e., SWI responses to dry and wet years), modeling catchment behavior during additional water years and in response to incrementally variable inputs, including phase, would provide further insight to historical and potential future SWI, and subsequent streamflow, dynamics at the rain-snow transition zone.

4.3.2. Implications

SWI is the variable that most directly controls soil moisture and thus subsurface water storage (Seyfried et al., 2009; Williams et al., 2009), groundwater recharge (Aishlin and McNamara, 2011; Scanlon et al., 2006), nutrient cycling (Schmidt and Lipson, 2004), and streamflow (Liu et al., 2013; McNamara et al., 2005; Moore et al., 1991). The use of the AWSM/iSnobal model generates a high-resolution (10–100 m), spatially distributed account of SWI, allowing this investigation of SWI drivers in space and through time.

SWI varied over one catchment in this work, and was generated from different locations in the catchment during different seasons and ROS events, depending on the local water and energy balance fluxes. Modeling and understanding the drivers of SWI on multiple temporal scales suggests that, in the rain-snow transition zone, as snowfall continues to decrease in a warming climate, redistribution of snowfall might also decrease, resulting in earlier snowmelt (Musselman et al., 2017; Badger et al., 2021). In turn, earlier snowmelt will result in more SWI earlier in the year and less SWI later in the year (Hale et al., 2022), potentially inducing water stress and differences in seasonal plant water use, if there is no summer rainfall to compensate (McNamara et al., 2005; Wieder et al., 2022). These deductions apply to both wet and dry water years, where the water and energy sensitivities at the rain-snow transition were similar across aspects and elevations, regardless of annual and seasonal precipitation magnitude. Thus, similar patterns in catchment responses to changes in climate may be expected in both wet and dry years.

The model allowed for a close examination of snow drifts; features strongly affecting SWI distribution in most catchments receiving snowfall in the mountainous western US (Ikeda et al., 2021). We show that this importance extends to the rain-snow transition zone, even though most snowpacks in this zone are relatively shallow and transient. Our results illuminate the importance of capturing snow drift formation in catchments to accurately capture the timing of catchment SWI and its origin across all temporal scales, consistent with similar work done in a nearby snow-dominated catchment (Luce et al., 1998) as well as in other regions (e.g., Brauchli et al., 2017). Yet, in the rain-snow transition zone in particular, previous analyses focused more on aspect controls than snow drifting and elevation controls on SWI (Kormos et al., 2014a, 2018). Additional works targeting SWI have not represented drifts due to model choice or spatial resolutions, or have represented drifts using a "drift factor" (Chauvin et al., 2011; Liu et al., 2013; Luce, 1998). Our work suggests that drifts, even in the rain-snow transition zone, are important in this region because they drive a strong relationship between annual precipitation and annual SWI (Fig. 4A and C), modulate SWI generation at seasonal timeframes and ROS events, create more heterogeneous SWE patterns across elevation bands via scour and deposition (Fig. 4B), and generate a substantial proportion of annual SWI in a small fraction of the catchment (Section 4.1). In addition to the importance of drifts in controlling the spatial and temporal patterns of SWI, drifts may be more sensitive to warming than the surrounding landscape (Marshall et al., 2019a). This might be especially true in mid-elevation mountains and at the rain-snow transition zone, which is shown to be highly sensitive to increases in atmospheric temperatures and changes in the present-day climate (Kormos et al., 2014a; Williams et al., 2009).

4.4. Conclusion

The purpose of this work was to evaluate the spatial patterns of surface water inputs (SWI; the summation of rainfall and snowmelt onto the soil), on annual, seasonal and event scales, across two water years, and to determine the driving forces of this primary water resource in the rain-snow transition zone of the western US. Annually, SWI distribution was driven primarily by precipitation in Johnston Draw across both a wet and dry water year. Snow drifts, covering approximately 3 % of the catchment area, generated the most SWI (8.0 % in 'wet' 2011 and 6.6 % in 'dry' 2014), highlighting the importance of snow drifts in SWI distribution. Conversely, high-elevation scoured areas produced the least amount of SWI across the defined aspect-elevation bins.

Seasonally, total energy fluxes were typically higher on the south- and other-facing slopes during mid-winter months, which coincided with early SWI generation (as snowmelt). Energy balance variables and SWI production increased on north-facing slopes and drift locations later in the spring and summer. At the ROS event scale, on average, more excess SWI was generated during events later in the year, where the snowpack was warmer and contained more liquid water and was near isothermal (i.e., "ripe" and warm). Across ROS events, more snowmelt occurred in the shallow, warm snowpacks before peak SWE, and on north-facing slopes and at higher elevations after peak SWE. Snow drifts were often too cold to produce snowmelt during ROS events, further demonstrating the importance of drifts as a significant regulator of SWI generation. As the climate continues to warm, the water inputs that drive SWI in the rain-snow transition zone will trend toward rainfall instead of snowfall. Not only will the snow line shift toward higher elevations, but the distribution and timing of SWI generation across the catchment might also change, affecting downstream streamflow dynamics and influencing the ecosystems and end-users that rely on seasonal snow water resources.

CRediT authorship contribution statement

K. Hale: Conceptualization, Data curation, Formal analysis, Funding acquisition, Investigation, Methodology, Resources, Validation, Visualization, Writing – original draft, Writing – review & editing. **L. Kiewiet:** Conceptualization, Data curation, Formal analysis, Investigation, Methodology, Resources, Validation, Visualization, Writing – original draft, Writing – review & editing. **E. Trujillo:** Data curation, Formal analysis, Methodology, Resources, Project administration, Validation, Supervision, Visualization, Writing – original draft, Writing – review & editing. **C. Krohe:** Methodology, Data curation, Resources, Writing – review & editing. **A. Hedrick:** Data curation, Formal analysis, Methodology, Resources, Project administration, Validation, Supervision, Visualization, Writing – original draft, Writing – review & editing. **D. Marks:** Data curation, Resources, Supervision, Project administration. **P. Kormos:** Resources, Writing – original draft, Revisions, Supervision, Project administration. **S. Havens:** Data curation, Formal analysis, Methodology, Resources, Project administration, Validation, Supervision, Visualization, Writing – original draft, Writing – review & editing. **J. McNamara:** Resources, Writing – original draft, Revisions, Supervision, Project administration. **T. Link:** Resources, Writing – original draft, Revisions, Supervision, Project administration. **S.E. Godsey:** Conceptualization, Data curation, Formal analysis, Investigation, Methodology, Resources, Validation, Visualization, Writing – original draft, Writing – review & editing.

Declaration of Competing Interest

The authors declare that they have no known competing financial interests or personal relationships that could have appeared to influence the work reported in this paper.

Data availability

Data will be made available on request.

Acknowledgments

USDA is an equal opportunity provider and employer. This research has been supported by the National Science Foundation Science Across Virtual Institutes (SAVI) project and NSF [IIA-1329469], the NSF Reynolds Critical Zone Observation Collaborative Agreement [58-5832-4-004], and the Swiss National Science Foundation [P2ZHP2_191376]. KH developed the concept of the study together with SEG, originally started by CK and SEG. LK, ET, AH, and SH performed and/or contributed to the simulations. KH prepared the first draft of the manuscript. All co-authors provided recommendations for the data analysis, participated in discussions about the results, and edited the manuscript.

Appendix A. Supplementary data

Supplementary data to this article can be found online at https://doi.org/10.1016/j.jhydrol.2022.128699.

References

Aishlin, P., McNamara, J.P., 2011. Bedrock infiltration and mountain block recharge accounting using chloride mass balance. Hydrol. Process. 25 (12), 1934–1948.

Anderton, S.P., White, S.M., Alvera, B., 2004. Evaluation of spatial variability in snow water equivalent for a high mountain catchment. Hydrol. Process. 18 (3), 435–453. https://doi.org/10.1002/hyp.1319.

Badger, A.M., Bjarke, N., Molotch, N.P., Livneh, B., 2021. The sensitivity of runoff generation to spatial snowpack uniformity in an alpine watershed: Green Lakes Valley, Niwot Ridge long-term ecological research station. Hydrol. Process. 35 (9), e14331.

Barnett, T.P., Adam, J.C., Lettenmaier, D.P., 2005. Potential impacts of a warming climate on water availability in snow-dominated regions. Nature 438 (7066), 303–309. https://doi.org/10.1038/nature04141.

Beniston, M., Stoffel, M., 2016. Rain-on-snow events, floods and climate change in the Alps: events may increase with warming up to 4 C and decrease thereafter. Sci. Total Environ. 571, 228–236.

Brauchli, T., Trujillo, E., Huwald, H., Lehning, M., 2017. Influence of slope-scale snowmelt on catchment response simulated with the Alpine3D model. Water Resour. Res. 53 (12), 10723–10739.

Brunengo, M.J., 2012. Where Is the Rain-on-Snow Zone in the West-Central Washington Cascades?: Monte Carlo Simulation of Large Storms in the Northwest. Portland State University.

Chauvin, G.M., Flerchinger, G.N., Link, T.E., Marks, D., Winstral, A.H., Seyfried, M.S., 2011. Long-term water balance and conceptual model of a semi-arid mountainous catchment. J. Hydrol. 400 (1–2), 133–143.

Cohen, J., Ye, H., Jones, J., 2015. Trends and variability in rain-on-snow events. Geophys. Res. Lett. 42 (17), 7115–7122.

Dozier, J., Bair, E.H., Davis, R.E., 2016. Estimating the spatial distribution of snow water equivalent in the world's mountains. Wiley Interdiscip. Rev.: Water 3 (3), 461–474.

Folland, C.K., Rayner, N.A., Brown, S.J., Smith, T.M., Shen, S.S.P., Parker, D.E., Sexton, D.M.H., 2001. Global temperature change and its uncertainties since 1861. Geophys. Res. Lett. 28 (13), 2621–2624.

Freudiger, D., Kohn, I., Stahl, K., Weiler, M., 2014. Large-scale analysis of changing frequencies of rain-on-snow events with flood-generation potential. Hydrol. Earth Syst. Sci. 18 (7), 2695–2709.

Fyfe, J., Derksen, C., Mudryk, L., et al., 2017. Large near-term projected snowpack loss over the western United States. Nat. Commun. 8, 14996. https://doi.org/10.1038/ncomms14996.

Garen, D.C., Marks, D., 2005. Spatially distributed energy balance snowmelt modelling in a mountainous river basin: estimation of meteorological inputs and verification of model results. J. Hydrol. 315 (1–4), 126–153.

Garvelmann, J., Pohl, S., Weiler, M., 2015. Spatio-temporal controls of snowmelt and runoff generation during rain-on-snow events in a mid-latitude mountain catchment. Hydrol. Process. 29 (17), 3649–3664.

Gergel, D.R., Nijssen, B., Abatzoglou, J.T., Lettenmaier, D.P., Stumbaugh, M.R., 2017. Effects of climate change on snowpack and fire potential in the western USA. Clim. Change 141 (2), 287–299.

Godsey, S.E., Marks, D., Kormos, P.R., Seyfried, M.S., Enslin, C.L., Winstral, A.H., et al., 2018. Eleven years of mountain weather, snow, soil moisture and streamflow data from the rain–snow transition zone – the Johnston Draw catchment, Reynolds creek experimental watershed and critical zone observatory, USA. Earth Syst. Sci. Data 10 (3), 1207–1216.

Guan, B., Waliser, D.E., Ralph, F.M., Fetzer, E.J., Neiman, P.J., 2016. Hydrometeorological characteristics of rain-on-snow events associated with atmospheric rivers. Geophys. Res. Lett. 43 (6), 2964–2973.

Hale, K.E., Wlostowski, A.N., Badger, A.M., Musselman, K.N., Livneh, B., Molotch, N.P., 2022. Modeling streamflow sensitivity to climate warming and surface water inputs in a montane catchment. J. Hydrol.: Reg. Stud. 39, 100976.

Hamlet, A.F., Mote, P.W., Clark, M.P., Lettenmaier, D.P., 2005. Effects of temperature and precipitation variability on snowpack trends in the western United States. J. Clim. 18 (21), 4545–4561.

Harpold, A.A., Kaplan, M.L., Klos, P.Z., Link, T., McNamara, J.P., Rajagopal, S., Schumer, R., Steele, C.M., 2017. Rain or snow: hydrologic processes, observations, prediction, and research needs. Hydrol. Earth Syst. Sci. 21, 1–22. https://doi.org/10.5194/hess-21-1-2017.

Hartman, M.D., Baron, J.S., Lammers, R.B., Cline, D.W., Band, L.E., Liston, G.E., Tague, C., 1999. Simulations of snow distribution and hydrology in a mountain basin. Water Resour. Res. 35 (5), 1587–1603.

Havens, H., Marks, D., Kormos, P., Hedrick, A., 2018. Spatial modeling for resources framework (SMRF): a modular framework for developing spatial forcing data for snow modeling in mountain basins. Comput. Geosci. 109 https://doi.org/10.1016/j.cageo.2017.08.016.

Havens, S., Marks, D., Sandusky, M., Hedrick, A., Johnson, M., Robertson, M., Trujillo, E., 2020. Automated water supply model (AWSM): streamlining and standardizing application of a physically based snow model for water resources and reproducible science. Comput. Geosci. 144, 104571.

Ikeda, K., Rasmussen, R., Liu, C., Newman, A., Chen, F., Barlage, M., Musselman, K., 2021. Snowfall and snowpack in the Western US as captured by convection permitting climate simulations: current climate and pseudo global warming future climate. Clim. Dyn. 1–25.

Jennings, K., Winchell, T., Livneh, B., Molotch, N.P., 2018. Spatial variation of the rain-snow temperature threshold across the Northern Hemisphere. Nat. Commun. 9 (1148) https://doi.org/10.1038/s41467-018-03629-7.

Jennings, K., Jones, J.A., 2015. Precipitation-snowmelt timing and snowmelt augmentation of large peak flow events, western Cascades, Oregon. Water Resour. Res. 51 (9), 7649–7661.

Julander, R.P., Clayton, J.A., 2018. Determining the proportion of streamflow that is generated by cold season processes versus summer rainfall in Utah, USA. J. Hydrol.: Reg. Stud. 17, 36–46.

Kiewiet, L., Trujillo, E., Hedrick, A., Havens, S., Hale, K., Seyfried, M., et al., 2022. Stream discharge depends more on the temporal distribution of water inputs than on yearly snowfall fractions for a headwater catchment at the rain-snow transition zone. Hydrol. Earth Syst. Sci. Discuss. 1–26.

Klos, P.Z., Link, T.E., Abatzoglou, J.T., 2014. Extent of the rain-snow transition zone in the western U.S. under historic and projected climate. Geophys. Res. Lett. https://doi.org/10.1002/2014GL060500.

Knowles, J.F., Harpold, A.A., Cowie, R., Zeliff, M., Barnard, H.R., Burns, S.P., et al., 2015. The relative contributions of alpine and subalpine ecosystems to the water balance of a mountainous, headwater catchment. Hydrol. Process. 29 (22), 4794–4808.

Kormos, Patrick R., Marks, Danny, Seyfried, Mark, Havens, Scott, Hedrick, Andrew, Lohse, Kathleen A., Masarik, Matt, Flores, Alejandro N., 2018. In: 31 Years of Spatially Distributed Air Temperature, Humidity, Precipitation Amount and Precipitation Phase from a Mountain Catchment in the Rain-snow Transition Zone. https://doi.org/10.18122/B2B59V.

Kormos, P.R., Marks, D., Williams, C.J., Marshall, H.P., Aishlin, P., Chandler, D.G., McNamara, J.P., 2014a. Soil, snow, weather, and sub-surface storage data from a mountain catchment in the rain–snow transition zone. Earth Syst. Sci. Data 6, 165–173. https://doi.org/10.5194/essd-6-165-2014.

Kormos, P., Marks, D., McNamara, J., Marshall, H., Winstral, A., Flores, A., 2014b. Snow distribution, melt and surface water inputs to the soil in the mountain rain–snow transition zone. J. Hydrol. 519, 190–204.

Kraft, M., McNamara, J., 2021. Evapotranspiration Across the Rain-Snow Transition in a Semi-Arid Watershed.

Kretchun, A.M., Scheller, R.M., Shinneman, D.J., Soderquist, B., Maguire, K., Link, T.E., Strand, E.K., 2020. Long term persistence of aspen in snowdrift-dependent ecosystems. For. Ecol. Manage. 462118005 https://doi.org/10.1016/j.foreco.2020.118005.

Kroczynski, S., 2004. A Comparison of Two Rain-on-snow Events and the Subsequent Hydrologic Responses in Three Small River Basins in Central Pennsylvania.

Kumar, M., Marks, D., Dozier, J., Reba, M., Winstral, A., 2013. Evaluation of distributed hydrologic impacts of temperature-index and energy-based snow models. Adv. Water Resour. 56, 77–89.

Lehning, M., Lo¨we, H., Ryser, M., Raderschall, N., 2008. Inhomogeneous precipitation distribution and snow transport in steep terrain. Water Resour. Res. 44 (7).

Liu, F., Hunsaker, C., Bales, R.C., 2013. Controls of streamflow generation in small catchments across the snow–rain transition in the Southern Sierra Nevada, California. Hydrol. Process. 27 (14), 1959–1972.

Lo´pez-Moreno, J.I., Pomeroy, J.W., Revuelto, J., Vicente-Serrano, S.M., 2013. Response of snow processes to climate change: spatial variability in a small basin in the Spanish Pyrenees. Hydrol. Process. 27 (18), 2637–2650.

Lo´pez-Moreno, J.I., Pomeroy, J.W., Mor´an-Tejeda, E., Revuelto, J., Navarro-Serrano, F. M., Vidaller, I., Alonso-Gonza´lez, E., 2021. Changes in the frequency of global high mountain rain-on-snow events due to climate warming. Environ. Res. Lett. 16 (9), 094021.

Luce, C.H., Tarboton, D.G., Cooley, K.R., 1998. The influence of the spatial distribution of snow on basin-averaged snowmelt. Hydrol. Process. 12 (10–11), 1671–1683. https://doi.org/10.1002/(SICI)1099-1085(199808/09)12:10/11<1671::AID-HYP688>3.0.CO;2-N.

Marks, D., Kimball, J., Tingey, D., Link, T., 1998. The sensitivity of snowmelt processes to climate conditions ans forest during rain on snow (SNOBAL). Hydrol. Process. 1587 (March), 1569–1587.

Marks, D., Domingo, J., Susong, D., Link, T., Garen, D., 1999. A spatially distributed energy balance snowmelt model for application in mountain basins. Hydrol. Process. 13, 1935–1959.
Marks, D., Link, T.E., Winstral, A., Garen, D., 2001. Simulating snowmelt processes during rain-on-snow over a semi-arid mountain basin. Ann. Glaciol. 32195–32202.
Marks, D., Winstral, A., 2001. Comparison of snow deposition, the snow cover energy balance, and snowmelt at two sites in a semiarid mountain basin. J. Hydrometeorol. 2 (3), 213–227.
Marks, D., Winstral, A., Reba, M., Pomeroy, J., Kumar, M., 2013. An evaluation of methods for determining during-storm precipitation phase and the rain/snow transition elevation at the surface in a mountain basin. Adv. Water Resour. 55, 98–110.
Marshall, A.M., Link, T.E., Abatzoglou, J.T., Flerchinger, G.N., Marks, D.G., Tedrow, L., 2019a. Warming alters hydrologic heterogeneity: simulated climate sensitivity of hydrology-based microrefugia in the snow-to-rain transition zone. Water Resour. Res. 55 (3), 2122–2141.
Marshall, A.M., Abatzoglou, J.T., Link, T.E., Tennant, C.J., 2019b. Projected changes in interannual variability of peak snowpack amount and timing in the western United States. Geophys. Res. Lett. 46 (15), 8882–8892.
McCabe, G.J., Clark, M.P., Hay, L.E., 2007. Rain-on-snow events in the western United States. Bull. Am. Meteorol. Soc. 88 (3), 319–328.
McNamara, J.P., Chandler, D., Seyfried, M., Achet, S., 2005. Soil moisture states, lateral flow, and streamflow generation in a semi-arid, snowmelt-driven catchment. Hydrol. Process.: Int. J. 19 (20), 4023–4038.
Molotch, N.P., Blanken, P.D., Link, T.E., 2011. Snow: Hydrological and Ecological Feedbacks in Forests, Forest Hydrology and Biogeochemistry. Springer, Dordrecht, pp. 541–555.
Moore, R.D., Owens, I.F., 1984. Modelling alpine snow accumulation and ablation using daily climate observations. J. Hydrol. (New Zealand) 73–83.
Moore, I.D., Grayson, R.B., Ladson, A.R., 1991. Digital terrain modelling: a review of hydrological, geomorphological, and biological applications. Hydrol. Process. 5 (1), 3–30.
Mote, P.W., Hamlet, A.F., Clark, M.P., Lettenmaier, D.P., 2005. Declining mountain snowpack in western North America. Bull. Am. Meteorol. Soc. 86 (1), 39–50.
Mote, P.W., Li, S., Lettenmaier, D.P., Xiao, M., Engel, R., 2018. Dramatic declines in snowpack in the western US. NPJ Clim. Atmos. Sci. 1 (1), 2. https://doi.org/10.1038/s41612-018-0012-1.
Musselman, K.N., Lehner, F., Ikeda, K., Clark, M.P., Prein, A.F., Liu, C., Barlage, M., Rasmussen, R., 2018. Projected increases and shifts in rain-on-snow flood risk over western North America. Nat. Clim. Change 8808–812. https://doi.org/10.1038/s41558-018-0236-4.
Musselman, K.N., Addor, N., Vano, J.A., Molotch, N.P., 2021. Winter melt trends portend widespread declines in snow water resources. Nat. Clim. Change 11 (5), 418–424.
Nayak, A.N.U.R.A.G., Marks, D., Chandler, D.G., Seyfried, M., 2010. Long-term snow, climate, and streamflow trends at the Reynolds Creek experimental watershed, Owyhee Mountains, Idaho, United States. Water Resour. Res. 46 (6).
Nolin, A.W., Daly, C., 2006. Mapping "at risk" snow in the Pacific Northwest. J. Hydrometeorol. 7 (5), 1164–1171.
Osterhuber, R., 1999. Precipitation intensity during rain-on-snow. In: Proc. 67th Western Snow Conf., South Lake Tahoe, CA, Western Snow Conference, pp. 153–155.
Patton, N.R., Lohse, K.A., Godsey, S.E., Crosby, B.T., Seyfried, M.S., 2018. Predicting soil thickness on soil mantled hillslopes. Nat. Commun. 9 (1), 1–10.
Pflug, J.M., Lundquist, J.D., 2020. Inferring distributed snow depth by leveraging snow pattern repeatability: investigation using 47 lidar observations in the Tuolumne watershed, Sierra Nevada, California. Water Resour. Res. 56 (9) e2020WR027243.
Pohl, S., Marsh, P., 2006. Modelling the spatial–temporal variability of spring snowmelt in an arctic catchment. Hydrol. Process.: Int. J. 20 (8), 1773–1792.
Pomeroy, J., Essery, R., Hardy, J., Rowlands, A., Marks, D., 2003. Uncertainty in estimating longwave fluxes to snow under forest canopies. In: EGS-AGU-EUG Joint Assembly, p. 12810.
Poulos, M.J., Smith, T.J., Benner, S.G., Pierce, J.L., Flores, A.N., Seyfried, M.S., McNamara, J.P., 2021. Topographically moderated soil water seasons impact vegetation dynamics in semiarid mountain catchments: illustrations from the dry creek experimental watershed, Idaho, USA. Hydrol. Process. https://doi.org/10.1002/hyp.14421.
Prowse, T.D., Owens, I.F., 1982. Energy balance over melting snow, Craigieburn Range, New Zealand. J. Hydrol. (New Zealand) 133–147.
Regonda, S.K., Rajagopalan, B., Clark, M., Pitlick, J., 2005. Seasonal cycle shifts in hydroclimatology over the western United States. J. Clim. 18 (2), 372–384.
Rücker, A., Boss, S., Kirchner, J.W., Freyberg, J.V., 2019. Monitoring snowpack outflow volumes and their isotopic composition to better understand streamflow generation during rain-on-snow events. Hydrol. Earth Syst. Sci. 23 (7), 2983–3005.
Scanlon, B.R., Keese, K.E., Flint, A.L., Flint, L.E., Gaye, C.B., Edmunds, W.M., Simmers, I., 2006. Global synthesis of groundwater recharge in semiarid and arid regions. Hydrol. Process.: Int. J. 20 (15), 3335–3370.
Schirmer, M., Wirz, V., Clifton, A., Lehning, M., 2011. Persistence in intra-annual snow depth distribution: 1. Measurements and topographic control. Water Resour. Res. 47 (9).
Schlo¨gl, S., Lehning, M., Mott, R., 2018. How are turbulent sensible heat fluxes and snow melt rates affected by a changing snow cover fraction? Front. Earth Sci. 6, 154.
Schmidt, S.K., Lipson, D.A., 2004. Microbial growth under the snow: implications for nutrient and allelochemical availability in temperate soils. Plant Soil 259 (1), 1–7.
Seyfried, M.S., Harris, R.C., Marks, D., Jacob, B., 2000 A geographic database for watershed research: Reynolds Creek Experimental Wa- tershed, Idaho, USA, Tech. Bull. NWRC 2000–3, Northwest Watershed Res. Cent., Agric. Res. Serv., U.S. Dep. of Agric., Boise, Idaho, 26 pp.
Seyfried, M., Harris, R.O.B.E.R.T., Marks, D.A.N.N.Y., Jacob, B., 2001. Geographic database, Reynolds Creek Experimental Watershed, Idaho. United States. Water Resources Research 37 (11), 2825–2829.
Seyfried, M., Flerchinger, G., Bryden, S., Link, T., Marks, D., McNamara, J., 2021. Slope and aspect controls on soil climate: field documentation and implications for large-scale simulation of critical zone processes. Vadose Zone J. https://doi.org/10.1002/vzj2.20158.
Seyfried, M.S., Grant, L.E., Marks, D., Winstral, A., McNamara, J.A.M.E.S., 2009. Simulated soil water storage effects on streamflow generation in a mountainous snowmelt environment, Idaho, USA. Hydrol. Process.: Int. J. 23 (6), 858–873.
Shakoor, A., Ejaz, N., 2019. Flow analysis at the snow-covered high-altitude catchment via distributed energy balance modeling. Sci. Rep. 9 (1), 1–14.
Shi, S., Liu, G., 2021. The latitudinal dependence in the trend of snow event to precipitation event ratio. Sci. Rep. 11 (1), 1–9.
Shrestha, R., Glenn, N.F., 2016. 2007 Lidar-Derived Digital Elevation Model, Canopy Height Model and Vegetation Cover Model Data Sets for Reynolds Creek Experimental Watershed, Southwestern Idaho.
Soderquist, B.S., Kavanagh, K.L., Link, T.E., Seyfried, M.S., Winstral Adam, H., A. h., 2018. Simulating the dependence of aspen (Populus tremuloides) on redistributed snow in a semi-arid watershed. Ecosphere 9 (1), 1–19. https://doi.org/10.1002/ecs2.2068.
St¨ahli, M., Jansson, P.E., Lundin, L.C., 1999. Soil moisture redistribution and infiltration in frozen sandy soils. Water Resour. Res. 35 (1), 95–103.
Stephenson, G.R., 1970. Soil-Geology-Vegetation Inventories for Reynolds Creek Watershed. Agric. Exp. Stn. Univ. Idaho Coll. Agric. USDA-ARS.
Steward, I.T., Cayan, D.R., Dettinger, M.D., 2005. Changes toward earlier streamflow timing across western North America. J. Clim. 18 (8), 1136–1155. https://doi.org/10.1175/JCLI3321.1.
Sturm, M., Wagner, A.M., 2010. Using repeated patterns in snow distribution modeling: an arctic example. Water Resour. Res. 46 (12).
Tinkham, W.T., Smith, A.M.S., Marshall, H.-P., Link, T.E., Falkowski, M.J., Winstral, A. H., 2014. Quantifying spatial distribution of snow depth errors from LiDAR using random forest. Remote Sens. Environ. 141105–115 https://doi.org/10.1016/j.rse.2013.10.021.
Trujillo, E., Havens, S., Hedrick, A.R., Johnson, M., Robertson, M., Pierson, F.B., Marks, D.G., 2019. Utilizing Spatially Resolved SWE to Inform Snowfall Interpolation Across a Headwater Catchment in the Sierra Nevada – AGU Fall Meeting. C33B-1579, bib code: 2019AGUFM.C33B1579T.
Vo¨egeli, C., Lehning, M., Wever, N., Bavay, M., 2016. Scaling precipitation input to spatially distributed hydrological models by measured snow distribution. Front. Earth Sci. 4, 108.
Wever, N., Fierz, C., Mitterer, C., Hirashima, H., Lehning, M., 2014. Solving Richards equation for snow improves snowpack meltwater runoff estimations in detailed multi-layer snowpack model. Cryosphere 8 (1), 257–274.
Wieder, W.R., Kennedy, D., Lehner, F., Musselman, K.N., Rodgers, K.B., Rosenbloom, N., et al., 2022. Pervasive alterations to snow-dominated ecosystem functions under climate change. Proceedings of the National Academy of Sciences 119 (30), e2202393119.
Williams, M.W., Seibold, C., Chowanski, K., 2009. Storage and release of solutes from a subalpine seasonal snowpack: soil and stream water response, Niwot Ridge, Colorado. Biogeochemistry 95 (1), 77–94. https://doi.org/10.1007/s10533-009-9288-x.
Winstral, A., Elder, K., Davis, R.E., 2002. Spatial snow modeling of wind-redistributed snow using terrain-based parameters. J. Hydrometeorol. 3 (5), 524–538.
Winstral, A., Marks, D., Gurney, R., 2013. Simulating wind-affected snow accumulations at catchment to basin scales. Adv. Water Resour. 55, 64–79.
Würzer, S., Jonas, T., Wever, N., Lehning, M., 2016. Influence of initial snowpack properties on runoff formation during rain-on-snow events. J. Hydrometeorol. 17 (6), 1801–1815.
Yang, Z.L., Dickinson, R.E., Hahmann, A.N., Niu, G.Y., Shaikh, M., Gao, X., Jin, J., 1999. Simulation of snow mass and extent in general circulation models. Hydrol. Process. 13 (12–13), 2097–2113.
Musselman, K.N., Clark, M.P., Liu, C., Ikeda, K., Rasmussen, R., 2017. Slower snowmelt in a warmer world. Nat. Clim. Change 7 (3), 214–219.